

Deep Extragalactic VISIBLE Legacy Survey (DEVILS): Stellar Mass Growth by Morphological Type since $z = 1$

Abdolhosein Hashemizadeh^{1*}, Simon P. Driver¹, Luke J. M. Davies¹,
Aaron S. G. Robotham¹, Sabine Bellstedt¹, Rogier A. Windhorst², Malcolm Bremer³,
Steven Phillipps³, Matt Jarvis^{4,5}, Benne W. Holwerda⁶, Claudia del P. Lagos¹,
Soheil Koushan¹, Malgorzata Siudek^{7,8}, Natasha Maddox⁹, Jessica E. Thorne¹,
Pascal Elahi¹

¹ICRAR, The University of Western Australia, 35 Stirling Highway, Crawley WA 6009, Australia

²School of Earth and Space Exploration, Arizona State University, Tempe, AZ 85287-1404

³Astrophysics Group, School of Physics, University of Bristol, Tyndall Avenue, Bristol BS8 1TL, UK

⁴Department of Astrophysics, University of Oxford, The Denys Wilkinson Building, Keble Road, Oxford OX1 3RH, UK

⁵Department of Physics, University of the Western Cape, Bellville 7535, South Africa

⁶Department of Physics and Astronomy, University of Louisville, Natural Science Building 102, 40292 KY Louisville, USA

⁷Institut de Física d'Altes Energies (IFAE), The Barcelona Institute of Science and Technology, 08193 Bellaterra (Barcelona), Spain

⁸National Centre for Nuclear Research, ul. Hoza 69, 00-681 Warsaw, Poland

⁹Faculty of Physics, Ludwig-Maximilians-Universität, Scheinerstr. 1, 81679 Munich, Germany

Accepted XXX. Received YYY; in original form ZZZ

ABSTRACT

Using high-resolution Hubble Space Telescope imaging data, we perform a visual morphological classification of $\sim 36,000$ galaxies at $z < 1$ in the DEVILS/COSMOS region. As the main goal of this study, we derive the stellar mass function (SMF) and stellar mass density (SMD) sub-divided by morphological types. We find that visual morphological classification using optical imaging is increasingly difficult at $z > 1$ as the fraction of irregular galaxies and merger systems (when observed at rest-frame UV/blue wavelengths) dramatically increases. We determine that roughly two-thirds of the total stellar mass of the Universe today was in place by $z \sim 1$. Double-component galaxies dominate the SMD at all epochs and increase in their contribution to the stellar mass budget to the present day. Elliptical galaxies are the second most dominant morphological type and increase their SMD by ~ 2.5 times, while by contrast, the pure-disk population significantly decreases by $\sim 85\%$. According to the evolution of both high- and low-mass ends of the SMF, we find that mergers and in-situ evolution in disks are both present at $z < 1$, and conclude that double-component galaxies are predominantly being built by the in-situ evolution in disks (apparent as the growth of the low-mass end with time), while mergers are likely responsible for the growth of ellipticals (apparent as the increase of intermediate/high-mass end).

Key words: galaxies: formation - galaxies: evolution - galaxies: bulges - galaxies: disk - galaxies: elliptical - galaxies: mass function - galaxies: structure - galaxies: general

1 INTRODUCTION

The galaxy population in the local Universe is observed to be bimodal. This bimodality manifests in multiple prop-

erties such as colour, morphology, metallicity, light profile shape and environment (e.g. Kauffmann et al. 2003; Baldry et al. 2004; Brinchmann et al. 2004). This bimodality is also found to extend to earlier epochs (see e.g., Strateva et al. 2001; Hogg et al. 2002; Bell et al. 2004; Driver et al. 2006; Taylor et al. 2009; Brammer et al. 2009; Williams et al.

* E-mail: abdolhosein.hashemizadeh@research.uwa.edu.au

2009; Brammer et al. 2011) across many measurable parameters, for example in colour (e.g. Cirasuolo et al. 2007; Cassata et al. 2008; Taylor et al. 2015), morphological type (e.g. Kelvin et al. 2014; Whitaker et al. 2015; Moffett et al. 2016; Krywult et al. 2017), size (e.g. Lange et al. 2015), and specific star formation rate (e.g. Whitaker et al. 2014; Renzini & Peng 2015 and the references therein). The inference from these observations is that there are likely two evolutionary pathways regulated by mass and environment giving rise to this bimodality (Driver et al. 2006; Scarlata et al. 2007b; De Lucia & Blaizot 2007; Peng et al. 2010; Trayford et al. 2016). However, it is unclear as to whether studying the global properties of galaxies or their individual morphological components can better explain the origin of this bimodality (Driver et al. 2013) or whether more complex astrophysics is required.

In this study, we explore the origin of this bimodality by using the global properties of galaxies to study the evolution of their stellar mass function (SMF). The SMF, a statistical tool for measuring and constraining the evolution of the galaxy population, is defined as the number density of galaxies per logarithmic mass interval (Schechter 1976). The SMF of galaxies in the local Universe is now very well studied and found to be described by a two-component Schechter (1976) function with a characteristic cut-off mass of between $10^{10.6}$ - $10^{11} M_{\odot}$ and a steepening to lower masses (for example see: Baldry et al. 2008; Peng et al. 2010; Baldry et al. 2012; Kelvin et al. 2014; Weigel et al. 2016; Moffett et al. 2016; Wright et al. 2017). Several studies have also investigated the evolution of the SMF at higher redshifts (Pozzetti et al. 2010; Muzzin et al. 2013; Whitaker et al. 2014; Leja et al. 2015; Mortlock et al. 2015; Wright et al. 2018; Kawinwanichakij et al. 2020). A fingerprint of this bimodality is also observed in the double-component Schechter function required to fit the local SMF (e.g. Baldry et al. 2012; Wright et al. 2018). At least two distinct galaxy populations corresponding to *star-forming* and *passive* systems are thought to be the origin of this bimodal shape, with *star-forming* systems dominating the low-mass tail and *passive* galaxies dominating the high-mass “hump” of the SMF (Baldry et al. 2012; Muzzin et al. 2013; Wright et al. 2018).

Many previous studies have separated galaxies into two main populations of star forming and passive (or a proxy thereof), and measured their individual stellar mass assemblies (e.g. Pozzetti et al. 2010; Tomczak et al. 2014; Leja et al. 2015; Davidzon et al. 2017). For example, by separating their sample into early- and late-type galaxies based on colour, Vergani et al. (2008) studied the SMF of the samples and confirmed that $\sim 50\%$ of the red sequence galaxies were already formed by $z \sim 1$. Pannella et al. (2006) used a sample of ~ 1600 galaxies split into early- intermediate- and late-type galaxies classified according to their Sérsic index. Similar work was carried out by Bundy et al. (2005) and Ilbert et al. (2010). In the local Universe, some studies have classified small samples of galaxies and investigated the SMF of different morphological types (Fukugita et al. 2007 and Bernardi et al. 2010 using The Sloan Digital Sky Survey, SDSS). For example Bernardi et al. (2010) reported that elliptical galaxies contain 25% of the total stellar mass density and 20% of the luminosity density of the local Universe.

Splitting galaxies into only two broad populations of star-forming and passive (or early- and late-type) galaxies

might be inadequate to comprehensively study all aspects of galaxy evolution (e.g., Siudek et al. 2018). Most previous studies at higher redshifts have separated galaxies into early- and late-type according to their colour distribution mainly due to the lack of spatial resolution as at high redshifts galaxies become unresolved in ground-based imaging. This has restricted true morphological comparisons in most studies to the local Universe (see e.g., Fontana et al. 2004; Baldry et al. 2004). A disadvantage of a simple colour-based classification is at higher redshifts, where for example regular disks occupied by old stellar populations are likely to be classified as early-type systems (see e.g., Pannella et al. 2006). This is however unlikely to have an impact on the visual morphological classification, particularly when using high resolution imaging such as the Hubble Space Telescope (HST) data (Huertas-Company et al. 2015). As such, we need better ways of quantifying the structure of galaxies throughout the history of the Universe. Consequently, some studies have started to probe visually classified morphological types (e.g., Sandage 2005; Fukugita et al. 2007; Nair & Abraham 2010; Lintott et al. 2011 and the references therein). In effect, there are two morphologies one might track: the end-point morphology at $z \sim 0$ or the instantaneous morphology at the observed epoch. Observing galaxies at higher redshifts we find a different distribution of morphological types. For example, in earlier works using HST, van den Bergh et al. (1996) and Abraham et al. (1996b) presented a morphological catalogue of galaxies in the Hubble Deep Field and found significantly more interacting, merger and asymmetric galaxies than in the nearby Universe.

By studying the SMF of various morphological types in the local Universe ($z < 0.06$), visually classified in the Galaxy and Mass Assembly survey (GAMA, Driver et al. 2011), Kelvin et al. (2014) and Moffett et al. (2016) found that the local stellar mass density is dominated by spheroidal galaxies, defined as E/S0/Sa. They reported the contribution of spheroid- (E/S0ab) and disk-dominated (Sbcd/Irr) galaxies of approximately 70% and 30%, respectively, towards the total stellar mass budget of the local Universe. These studies, however, are limited to the very local Universe. For a better understanding of the galaxy formation and evolution processes at play in the evolution of different morphological types, and their rates of action, we need to extend similar analyses to higher redshifts. This will allow us to explore the contribution of different morphological types to the stellar mass budget as a function of time and elucidate the galaxy evolution process.

In the present work, we perform a visual morphological classification of galaxies in the DEVILS-D10/COSMOS field (Scoville et al. 2007; Davies et al. 2018). We make use of the high resolution HST imaging and use a sample of galaxies within $0 \leq z \leq 1$ and $M_{*} > 10^{9.5}$, selected from the DEVILS sample and analysis, for which classification is reliable. This intermediate redshift range is a key phase in the evolution of the Universe where a large fraction ($\sim 50\%$) of the present-day stellar mass is formed and large structures such as groups, clusters and filaments undergo a significant evolution (Davies et al. 2018). During this period the sizes and masses of galaxies also appear to undergo significant evolution (e.g. van der Wel et al. 2012).

By investigating the evolution of the SMF for different morphological types across cosmic time we can probe

the various systems within which stars are located, and how they evolve. In this paper, we investigate the evolution of the stellar mass function of different morphological types and explore the contribution of each morphology to the global stellar mass build-up of the Universe. Shedding light on the redistribution of stellar mass in the Universe and also the transformation and redistribution of the stellar mass between different morphologies likely explains the origin of the bimodality in galaxy populations observed in the local Universe.

The ultimate goal of this study and its companion papers is to not only probe the evolution of the morphological types but also study the formation and evolution of the galaxy structures, including bulges and disks. This will be presented in a companion paper (Hashemizadeh et al. in prep.), while in this paper we explore the visual morphological evolution of galaxies and conduct an assessment into the possibility of the bulge formation scenarios by constructing the global stellar mass distributions and densities of various morphological types.

The data that we use in this work are presented in Section 8. In Section 1.3, we define our sample and sample selection. Section 2 presents different methods that we explore for the morphological classification. In Section 3, we describe the parameterisation of the SMF. We then show the *total* SMF at low- z in Section 3.1. Section 3.2 describes the effects of the cosmic large scale structure due to the limiting size of the DEVILS/COSMOS field, and the technique we use to correct for this. The evolution of the SMF and the SMD and their subdivision by morphological type are discussed in Sections 3.3-4. We finally discuss and summarize our results in Sections 5-6.

Throughout this paper, we use a flat standard Λ CDM cosmology of $\Omega_M = 0.3$, $\Omega_\Lambda = 0.7$ with $H_0 = 70 \text{ km s}^{-1} \text{ Mpc}^{-1}$. Magnitudes are given in the AB system.

1.1 DEVILS: Deep Extragalactic Visible Legacy Survey

The Deep Extragalactic Visible Legacy Survey (DEVILS) (Davies et al. 2018), is an ongoing magnitude-limited spectroscopic and multi-wavelength survey. Spectroscopic observations are currently being undertaken at the Anglo-Australian Telescope (AAT), providing spectroscopic redshift completeness of $> 95\%$ to $Y\text{-mag} < 21.2$ mag. This spectroscopic sample is supplemented with robust photometric redshifts, newly derived photometric catalogues (Davies et al. in prep.) and derived physical properties (Thorne et al. 2020, and the work here) all undertaken as part of the DEVILS project. These catalogues extend to $Y \sim 25$ mag in the D10 region.

The objective of the DEVILS campaign is to obtain a sample with high spectroscopic completeness extending over intermediate redshifts ($0.3 < z < 1.0$). At present, there is a lack of high completeness spectroscopic data in this redshift range (e.g., Davies et al. 2018; Scodreggio et al. 2018). DEVILS will fill this gap and allow for the construction of group, pair and filamentary catalogues to fold in environmental metrics. The DEVILS campaign covers three well-known fields: the XMM-Newton Large-Scale Structure field (D02: XMM-LSS), the Extended Chandra Deep Field-South (D03: ECDFS), and the Cosmological Evolution Survey field (D10:

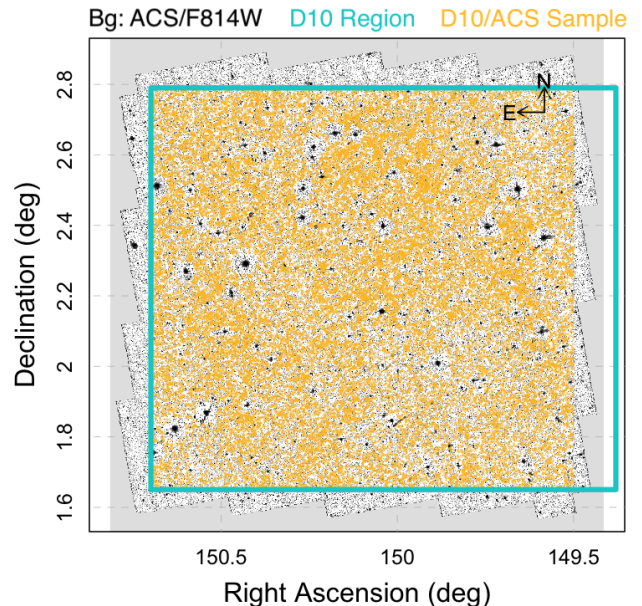


Figure 1. Background shows the ACS/F814W mosaic image of the COSMOS field. The cyan rectangle represents the D10 region in the DEVILS survey. Gold points are the D10/ACS sources used in this work consisting of $\sim 36\text{k}$ galaxies. See section 1.3 for more detail.

COSMOS). In this work, we only explore the D10 region as this overlaps with the HST COSMOS imaging. The spectroscopic redshifts used in this paper are from the DEVILS combined spectroscopic catalogue which includes all available redshifts in the COSMOS region, including zCOSMOS (Lilly et al. 2007, Davies et al. 2015), hCOSMOS (Damjanov et al. 2018) and DEVILS (Davies et al. 2018). As the DEVILS survey is ongoing the spectroscopic observations for our full sample are still incomplete (the completeness of the DEVILS combined data is currently ~ 90 per cent to $Y\text{-mag} = 20$). Those objects without spectroscopic redshifts are assigned photometric redshifts in the DEVILS master redshift catalogue (DEVILS_D10MasterRedshiftCat.v0.2 catalogue), described in detail in Thorne et al. (2020). In this work, we also use the stellar mass measurements for the D10 region (DEVILS_D10ProSpectCat.v0.3 catalogue) reported by Thorne et al. (2020). Briefly, to estimate stellar masses they used the PROSPECT SED fitting code (Robotham et al. 2020) adopting Bruzual & Charlot (2003) stellar libraries, the Chabrier (2003) IMF together with Charlot & Fall (2000) to model dust attenuation and Dale et al. (2014) to model dust emission. This study makes use of the new multiwavelength photometry catalogue in the D10 field (DEVILS_PhotomCat.v0.4; Davies et al. in prep.) and finds stellar masses ~ 0.2 dex higher than in COSMOS2015 (Laigle et al. 2016) due to differences in modelling an evolving gas phase metallicity. See Thorne et al. (2020) for more details.

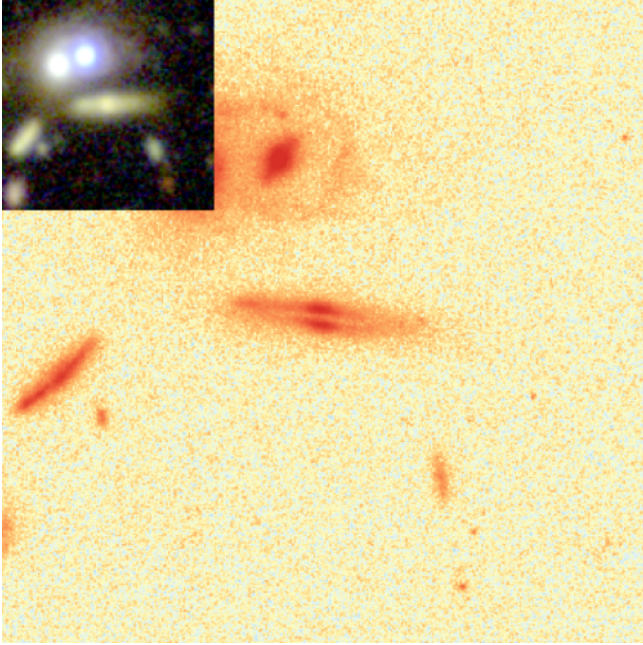


Figure 2. A random galaxy in our sample at redshift $z \sim 0.47$ showing an example of the postage stamps we generate to perform our visual inspection. Main image is the HST ACS/F814W and the inset is SUBARU *gri* colour image. The image shows a cutout of $5 \times R90$ on each side, where $R90 = 3.23$ arcsec measured from UltraVISTA Y-band (Davies et al. 2018).

1.2 COSMOS ACS/WFC imaging data

The Cosmic Evolution Survey (COSMOS) is one of the most comprehensive deep-field surveys to date, covering almost 2 contiguous square degrees of sky, designed to explore large scale structures and the evolution of galaxies, AGN and dark matter (Scoville et al. 2007). The high resolution Hubble Space Telescope (HST) F814W imaging in COSMOS allows for the study of galaxy morphology and structure out to the detection limits. In total COSMOS detects ~ 2 million galaxies at a resolution of < 100 pc (Scoville et al. 2007).

The COSMOS region is centred at RA = 150.121 (10 : 00 : 28.600) and DEC = +2.21 (+02 : 12 : 21.00) (J2000) and is supplemented by 1.7 square degrees of imaging with the Advanced Camera for Surveys (ACS¹) on HST. This 1.7 square degree region was observed during 590 orbits in the F814W (I-band) filter and also, 0.03 square degrees with F475W (g-band). In this study we exclusively use the F814W filter, not only providing coverage but also suitable rest-frame wavelength for the study of optical morphology of galaxies out to $z \sim 1$ (Koekemoer et al. 2007). The original ACS pixel scale is 0.05 arcsec and consists of a series of overlapping pointings. These have been drizzled and re-sampled to 0.03 arcsec resolution using the MultiDrizzle code (Koekemoer et al. 2003), which is the imaging data we use in this work. The frames were downloaded from the public NASA/IPAC Infrared Science Archive (IRSA) webpage² as fits images.

1.3 Sample selection: D10/ACS Sample

As part of the DEVILS survey we have selected an HST imaging sample with which to perform various morphological and structural science projects. Figure 1, shows the ACS mosaic imaging of the COSMOS field with the full D10 region overlaid as a cyan rectangle (defined from the Ultra VISTA imaging). Our final sample, D10/ACS, is the common subset of sources from ACS and D10. The position of the D10/ACS sample on the plane of RA and DEC is overplotted on the same figure as yellow dots. Note that as shown in Figure 1, we exclude objects in the jagged area of the ACS imaging leading to a rectangular effective area of 1.3467 square degrees.

Although our HST imaging data is high resolution (see Figure 2 for a random galaxy at redshift $z \sim 0.47$), we are still unable to explore galaxy morphologies beyond a certain redshift and stellar mass in our analysis as galaxies become too small in angular scale or too dim in surface brightness to identify morphological substructures.

We first try to select a complete galaxy sample from the DEVILS-D10/COSMOS data to define the redshift and stellar mass range for which we can perform robust morphological classification and structural decomposition (Hashemizadeh et al. in prep.). Note that we make use of a combination of photometric and available spectroscopic redshifts as well as stellar masses as described in Section 1.1. In total, at the time of writing this paper, 23,264 spectroscopic redshifts are available in the D10 region (excluding the jagged edges) out of which 2,903 redshifts are observed by DEVILS. See the DEVILS website³ for a full description of these data. We select 284 random galaxies drawn from across the entire redshift and stellar mass distribution, and visually inspect them. These 284 galaxies are shown as circles in Figure 3. From our visual inspection, we identify the boundaries within which we believe the majority of galaxies are sufficiently resolved that morphological classifications should be possible (i.e., not too small or faint). Our visual assessments are indicated by colour in Figure 3 showing two-component (grey), single component (blue), and problematic cases (red; merger, disrupted, and low S/N). Unsurprisingly, in agreement with other studies (e.g. Conselice et al. 2005), we find the fraction of problematic galaxies increases drastically at high redshifts ($z > 1.4$). Beyond this redshift an increasing number of galaxies ($\sim 50\%$) become complex and no longer adhere to a simplistic picture of a central bulge plus disk system. A large fraction of galaxies appear interacting, clumpy, very faint and/or extremely *compact*, hence the notion of galaxies as predominantly bulge plus disk systems becomes untenable. Note that the vast majority of galaxies in this redshift range are disturbed interacting systems, however our observation of a fraction of the clumpy galaxies could be due to the fact that the bluer rest-frame emission is more sensitive to star forming regions dominating the flux. The clumps and potential bulges at this epoch, are mostly comparable or smaller than the HST PSF, hence conventional 2D bulge+disk fits are also unlikely to be credible even at HST resolution.

¹ ACS Hand Book: www.stsci.edu/hst/acs/documents/

² irsa.ipac.caltech.edu/data/COSMOS/images/acs.2.0/I/

³ <https://devilsurvey.org>

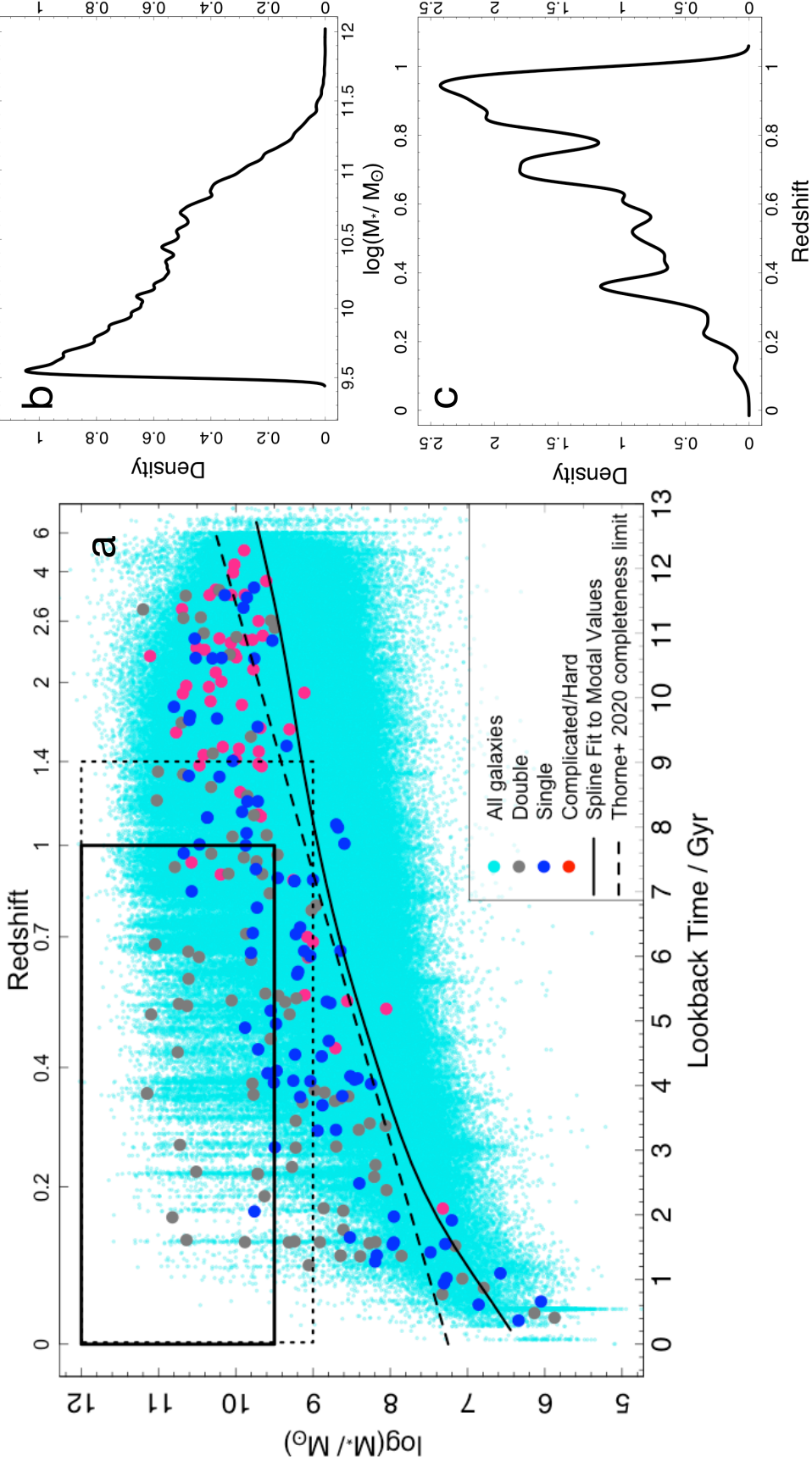


Figure 3. (a) The relation between stellar mass and lookback time (redshift) of our sample. All galaxies are shown in cyan in background. Circles represent 284 galaxies that we randomly sample for initial visual inspection. Grey and blue circles show double and single component galaxies, respectively. Red symbols are complicated galaxies which consist of merging systems, perturbed galaxies, low S/N or high redshift clumpy galaxies. The dotted rectangle corresponds to our initial sample region ($z < 1.4$ and $\log(M_*/M_\odot) > 9$). The solid rectangle shows our final sample region which covers galaxies up to $z < 1.0$ and $\log(M_*/M_\odot) > 9.5$. The solid black line represents the spline fit to the modal value of the stellar mass in bins of lookback time indicating the stellar mass completeness. Black dashed line shows Thorne et al. (2020) completeness limit. See text for more details. Panels (b) and (c) display the distribution of stellar mass and redshift of our final sample (i.e. within the solid rectangle). Note that the PDFs are smoothed by a kernel with standard deviation of 0.02.

Note that as can be seen in Figure 3, we also start to suffer significant mass incompleteness at low redshifts due to the COSMOS F814W sensitivity limit. The sample completeness limit is shown here as a smooth spline fitted to the modal values of stellar mass in bins of lookback time (shown as a solid line), i.e., peaks of the stellar mass histograms in narrow redshift slices. We also show the completeness limit reported by Thorne et al. (2020) and shown as a dashed line in Figure 3, which is based on a $g-i$ colour analysis and is formulated as $\log(M_*) = 0.25t + 7.25$, where t is lookback time in Gyr. From this initial inspection we define our provisional window of 105,185 galaxies at $z < 1.4$ and $\log(M_*/M_\odot) > 9$, shown as a dotted rectangle in Figure 3.

To further tune this selection, we then generated postage stamps of 4,000 random galaxies (now initial selection) using the HST F814W imaging and colour gri insets from the Subaru Suprime-Cam data (Taniguchi et al. 2007). Figure 2 shows an example of the cutouts we generated for our visual inspection. The postage stamps are generated with $5 \times R90$ on each side, where $R90$ is the radius enclosing 90% of the total flux in the UltraVISTA Y-band (soon to be presented in DEVILS photometry catalogue, Davies et al. in prep.). These stamps were independently reviewed by five authors (AH, SPD, ASGR, LJMD, SB) and classified into single component, double component and complicated systems (hereafter: *hard*). The single component systems were later subdivided into disk or elliptical systems. Note that the *hard* class consists of asymmetric, merging, clumpy, extremely compact and low-S/N systems, for which 2D structural decomposition would be unlikely to yield meaningful output. Objects with three or more votes in one category were adopted and more disparate outcomes discussed and debated until an agreement was obtained. In this way, we established a “gold calibration sample” of 4k galaxies to justify our final redshift and stellar mass range, and for later use as a training sample in our automated-classification process, see Section 2 for more details.

Figure 4 shows the fraction of each of the above classifications versus redshift and total stellar mass (dashed lines). As the left panel shows, the fraction of *hard* galaxies (gray dashed line) drastically increases at $z > 1$. At the highest redshift of our sample, $z \sim 1.4$, 40 percent of the galaxies are deemed unfittable, or at least inconsistent with the notion of a classical/pseudo-bulge plus disk systems (this is consistent with Abraham et al. 1996a and Conselice et al. 2005). Also see the review by Abraham & van den Bergh (2001). We therefore further restrict our redshift range to $z \leq 1$ in our full-sample analysis. Additionally, we increase our stellar mass limit to $\log(M_*/M_\odot) = 9.5$ to reduce the effects of incompleteness (see Figure 3) and to restrict our sample to a manageable number for morphological classifications. In Figure 3, our final sample selection region is now shown as a solid rectangle. The distribution of the stellar mass and redshift of our final sample is also displayed in the right panels (b and c) of the same figure.

Overall, our analysis of galaxies in different regions of the M_* - z parameter space leads us to a final sample of galaxies for which we can confidently study their morphology and structure. We conclude that we can study the structure of galaxies up to $z \sim 1$ and down to $\log(M_*/M_\odot) \geq 9.5$. Within this selection, our sample consists of 35,803 galaxies with 14,036 available spectroscopic redshifts.

2 FINAL MORPHOLOGICAL CLASSIFICATIONS

In this section, we initially aim to develop a semi-automatic method for morphological classification. Our ultimate goal would be to reach a fully automatic algorithm for classifying galaxies into various morphological classes. While this ultimately proves unsuitable we discuss it here to explain why we finally visually inspect all systems. These classes are as mentioned above *bulge+disk* (BD; double-component), *pure-disk* (D), *elliptical* (E) and *hard* (H) systems. In order to overcome this problem we test various methods including: cross-matching with Galaxy Zoo, Hubble catalogue (GZH) and Zurich Estimator of Structural Type (ZEST) catalogues. In the end, none of the methods proved to be robust and we resort to full visual inspection.

2.1 Using Galaxy Zoo: Hubble

A large fraction of COSMOS galaxies with $I_{F814W} < 23.5$ have been classified in the Galaxy Zoo: Hubble (GZH) project (Willett et al. 2017). Like other Galaxy Zoo projects, this study classifies galaxies using crowdsourced visual inspections. They make use of images taken by the ACS in various wavelengths including 84,954 COSMOS galaxies in the F814W filter. Our sample has more than 80% overlap with GZH, so we can cross-match and use their classifications to partially improve our final sample. We translate the GZH classifications into our desired morphological classes by using the decision tree shown in figure 4 of Willett et al. (2017), as well as the suggested thresholds for morphological selection presented in Table 11 of the same paper. Our final decision tree is displayed in the flowchart shown in Figure 5. We refer to Willett et al. (2017) for a detailed description of each task. The thresholds are shown as P values in the flowchart. In addition to using different combinations and permutations of tasks as shown in Figure 5, the only part that we add to the GZH tasks is where an object is voted to have a smooth light profile. In this case, the object is likely to be an E or S0 or a smooth *pure-disk* galaxy. To distinguish between them, we make use of the single Sérsic index (n). As shown in the flowchart, $n > 2.5$ and $n \leq 2.5$ are classified as spheroid and *pure-disk*, respectively. The Sérsic indices are taken from our structural analysis which will be described in Hashemizadeh et al. (in prep.). In order to capture the S0 galaxies or *double-component* systems with smooth disk profiles we add an extra condition as to whether there are at least 2 Galaxy Zoo votes for a prominent bulge. If so then it is likely that the galaxy is a *double-component* system. An advantage of using the GZH decision tree is that it can identify a vast majority of galaxies with odd features such as merger-induced asymmetry etc. Table 1 shows a confusion matrix comparing the GZH predictions with the visual inspection of our 4k gold sample as the ground truth. Double component galaxies are predicted by the GZH with maximum accuracy 81%. Single component (i.e. *pure-disk* and *elliptical* galaxies) and *hard* galaxies are predicted at a significantly lower accuracy with high misclassification rates. We further visually inspected misclassified galaxies and do not find good agreement between our classification and those of GZH. As such, we do not trust the GZH classification for our sample.

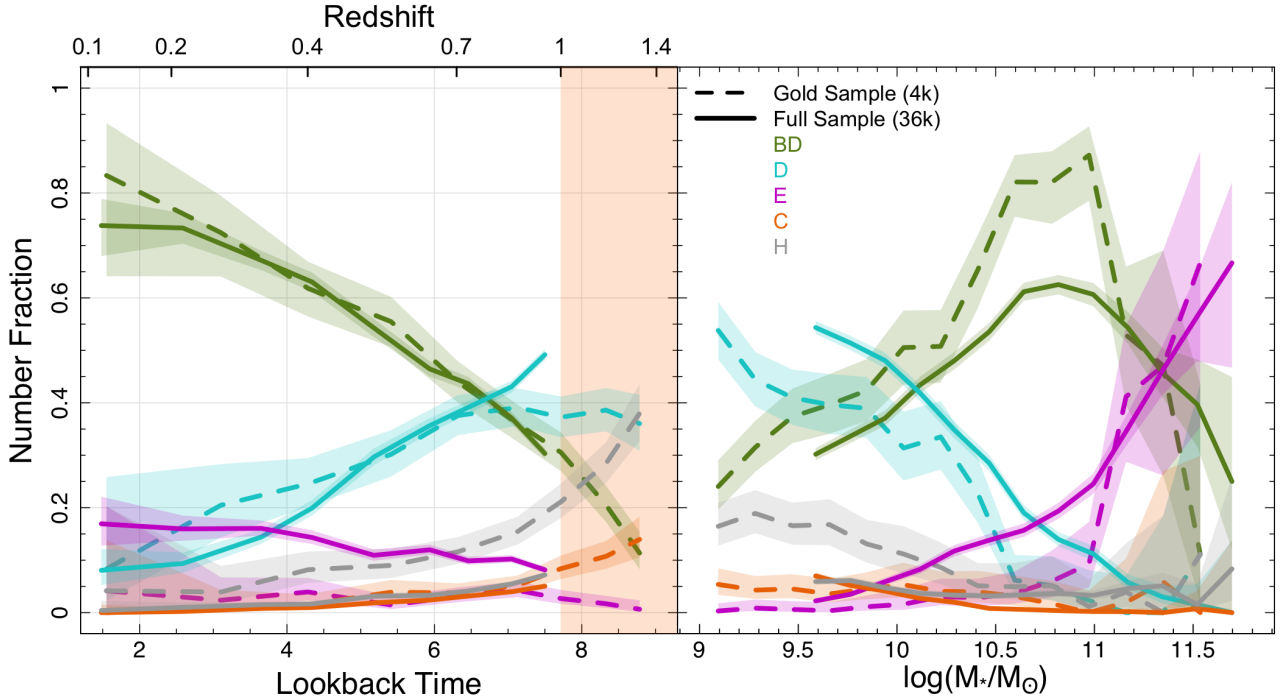


Figure 4. The number fraction of each morphological type (BD: *bulge+disk*, D: *pure-disk*, E: *elliptical*, C: *compact*, H: *hard*) in bins of lookback time (redshift) and total stellar mass, left and right panels, respectively. Each colour represents a morphology as indicated in the inset legend. Dashed lines are the ~ 4000 random sample that we visually classified ($z < 1.4$) while solid lines are our full visual inspection of the final sample. Shaded stripes around lines display 95% confidence intervals from beta distribution method as calculated using `prop.test` in R package `stats`.

2.2 Using Zurich Estimator of Structural Type (ZEST)

Another available morphological catalogue for COSMOS galaxies is the Zurich Estimator of Structural Type (ZEST) (Scarlata et al. 2007a). In ZEST, Scarlata et al. (2007a) use their single-Sérsic index (n) as well as five other diagnostics: asymmetry, concentration, Gini coefficient, second-order moment of the brightest 20% of galaxy flux, and ellipticity. ZEST includes a sample of $\sim 56,000$ galaxies with $I_{F814W} \leq 24$. More than 90% of our sample is cross-matched with ZEST which we use as a complementary morphological classification. We use the ZEST TYPE flag with four values of 1,2,3,9 representing early type galaxy, disk galaxy, irregular galaxy and no classification. For Type 2 (i.e. disk galaxy) we make use of the additional flag BULG, which indicates the level of bulge prominence. BULG is flagged by five integers as follows: 0 = bulge dominated, 1,2 = intermediate-bulge, 3 = *pure-disk* and 9 = no classification. We present the accuracy of ZEST predictions in a confusion matrix in Table 2 which shows we do not find an accurate morphological prediction from ZEST in comparison to our gold calibration sample. While *double-component* systems are classified with an accuracy of 74%, other classes are classified poorly with high error ratios. We confirm this by visual inspection of the misclassified objects where we still favour our visual classification.

Table 1. The confusion matrix comparing the morphological predictions of the GZH with our visual inspection of 4k gold calibration sample as the ground truth. For example, 0.81 means 81% of double component galaxies (in our visual classification) are also correctly classified by the GZH.

GZH Pred \ Ground Truth			
	Double	Hard	Single
Double	0.81	0.28	0.32
Hard	0.0038	0.18	0.011
Single	0.18	0.53	0.67

Overall, by analysing both of the above catalogues we do not find them to be sufficiently accurate for predicting the proper morphologies of galaxies when we compare their estimates with our 4k gold calibration visual classification.

2.3 Visual inspection of full D10/ACS sample

As no automatic classification robustly matches our gold calibration sample we opt to visually inspect all galaxies in our full sample. However, we can use the predictions from GZH and ZEST as a pre-classification decision and put galaxies in master directories according to their prediction. The *hard* class is adopted from the GZH prediction as it is shown to perform well in detecting galaxies with odd features. In addi-

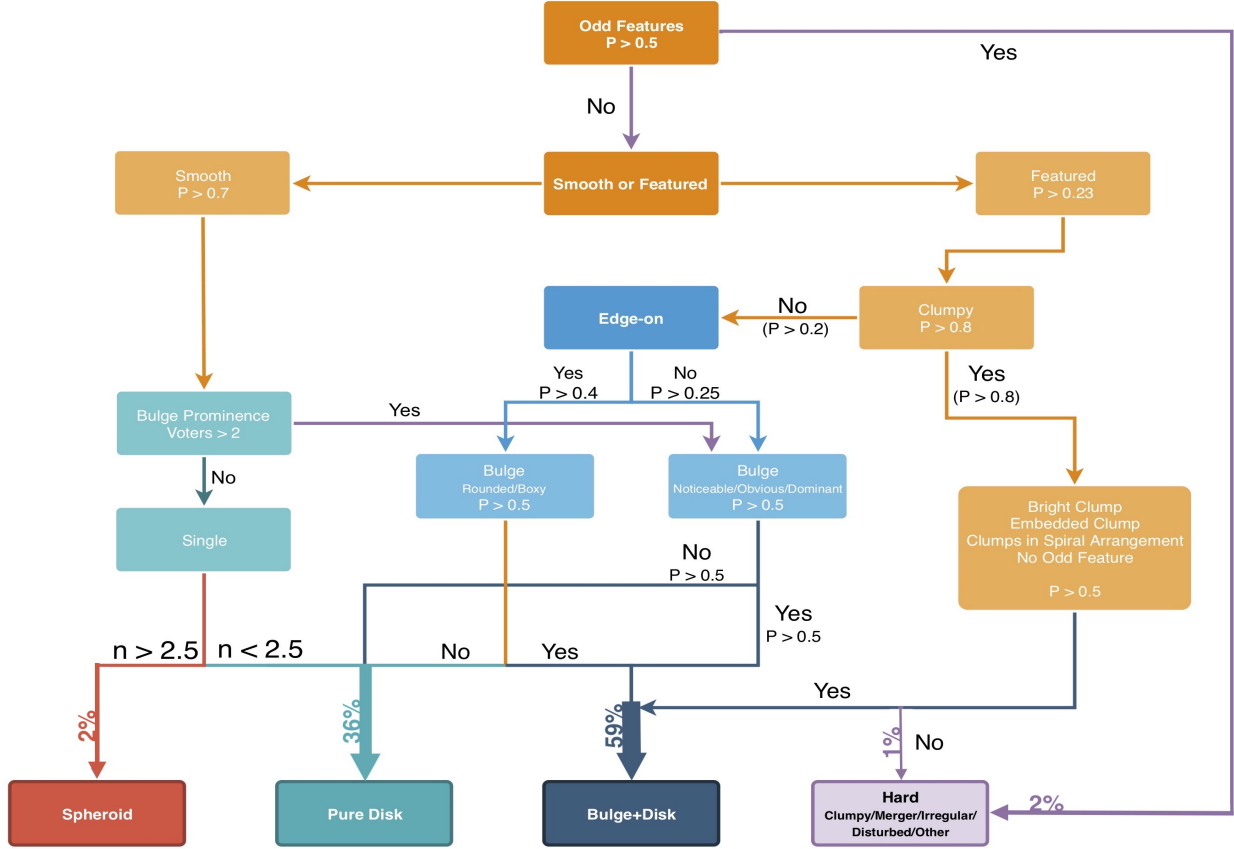


Figure 5. This flowchart shows the decision tree that we adopt to translate Galaxy Zoo: Hubble (GZH) tasks and outputs into the desired morphologies to be used in this study. The weight of final arrows are proportional to the number of galaxies following those paths. In addition, the fraction of galaxies falling into each morphological category is annotated.

Table 2. The confusion matrix comparing the morphological predictions of the ZEST catalogue with our visual inspection of 4k gold calibration sample as the ground truth.

ZEST Pred \ Ground Truth			
	Double	Hard	Single
Double	0.74	0.34	0.42
Hard	0.047	0.37	0.036
Single	0.21	0.28	0.55

tion, from analysing the distribution of the half-light radius (R_{50}) of our 4k gold calibration sample, extracted from our DEVILS photometric analysis, we know that resolving the structure of galaxies with a spatial size of $R_{50} \leq 0.15$ arcsec is nearly impossible. R_{50} is measured by using the PROFOUND package (Robotham et al. 2018), a tool written in the R language for source finding and photometric analysis. So, we put these galaxies into a separate *compact* class (C).

Having pre-classified galaxies, we now assign each class to one of our team members (AH, SPD, ASGR, LJMD, SB) so each of the authors is independently a specialist in, and responsible for, only one morphological class. Initially, we inspect galaxies and relocate incorrectly classified galaxies from our master directories to transition folders for

further inspections by the associated responsible person. In the second iteration, the incorrectly classified systems will be reclassified and moved back into master directories. The left-over sources in the transition directories are therefore ambiguous. For these galaxies, all classifiers voted and we selected the most voted class as the final morphology. As a final assessment and quality check three of our authors (SPD, LJMD, SB) independently reviewed the entire classifications ($\sim 15k$ each) and identified $\sim 7k$ that were still felt to be questionable. These three classifiers then independently classified these 7k objects. The final classification was either the majority decision or in the case of a 3-way divergence the classification of SPD.

Figure 6 shows the stellar mass versus redshift plane colour coded according to the level of agreement between our 3 classifiers. Colour indicates the percentage of objects in each cell consistently classified by at least two classifiers, obtained as follows:

$$\text{Agreement} = \frac{\text{Number of objects with two or more agreement in the cell}}{\text{Total number of objects in the cell}}, \quad (1)$$

This figure implies that we have the highest agreement ($\sim 100\%$) for high stellar mass objects at low redshifts. The agreement in our classification decreases to $\sim 90\% - 95\%$ towards lower stellar mass regime at high redshift. This fig-

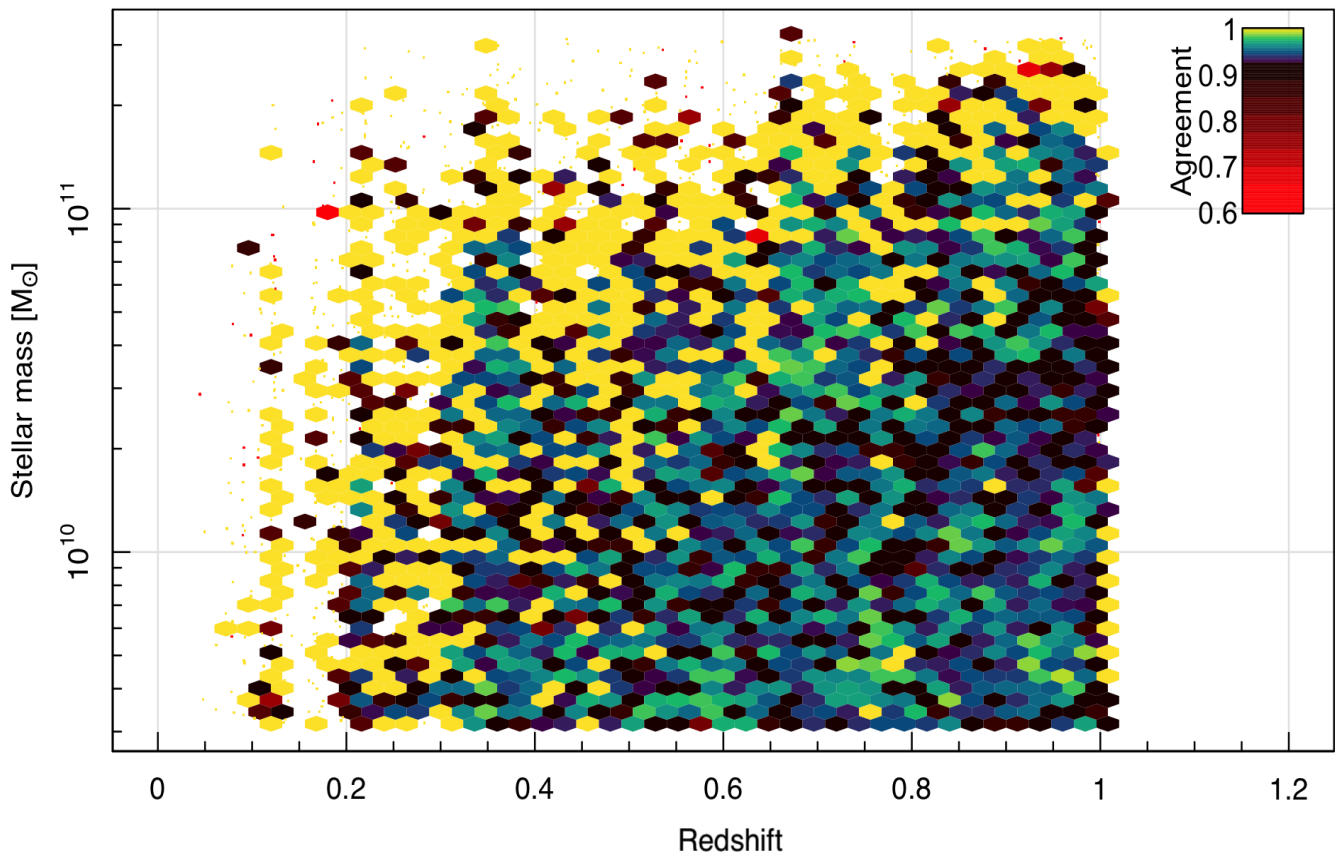


Figure 6. Stellar mass versus redshift, colour coded by the level of agreement in our final classifications (by three co-authors), i.e. the percentage of objects in each cell consistently classified by at least two of our classifiers. Note that we increase the resolution of the colour map of agreement $\gtrsim 0.92$ to highlight the variation of agreement in this level. See the text for more details.

ure indicates that, on average, our visual classifications performed independently by different team members agree by $\sim 95\%$ over the complete sample.

We report the number of objects in each morphological class in Table 3. 44.4% of our sample (15,931) are classified as *double-component* (BD) systems. We find 13,212 *pure-disk* (D) galaxies (37%) while only 3,890 (11%) *elliptical* (E) galaxies. The *Compact* (C) and *hard* (H) systems, in total, occupy 7.6% of our D10/ACS sample.

The visual morphological classification is released in the team-internal DEVILS data release one (DR1) in D10VisualMoprholoCat data management unit (DMU).

2.4 Possible effects from the “Morphological K-correction” on our galaxy classifications

The morphology of a subset of nearby galaxy classes shows some significant dependence on rest-frame wavelengths, especially below the Balmer break and towards the UV (e.g. Hibbard & Vacca 1997; Windhorst et al. 2002; Papovich et al. 2003; Taylor et al. 2005; Taylor-Mager et al. 2007; Huertas-Company et al. 2009; Rawat et al. 2009; Holwerda et al. 2012; Mager et al. 2018). This “Morphological K-correction” can be quite significant, even between the B- and near-IR bands (e.g., Knapen & Beckman 1996), and must be quantified in order to distinguish genuine evolutionary

effects from simple bandpass shifting. Hence, the results of faint galaxy classifications may, to some extent, depend on the rest-frame wavelength sampled.

Our D10/ACS classifications are done in the F814W filter (I-band), and the largest redshift in our sample, $z \sim 1$, samples ~ 412 nm (B-band), so for our particular case, the main question is, to what extent galaxy rest-frame morphology changes significantly from 412–823 nm across the BVRI filters. Here we briefly summarize how any such effects may affect our classifications.

Windhorst et al. (2002) imaged 37 nearby galaxies of all types with the Hubble Space Telescope (HST), gathering available data mostly at 150, 255, 300, 336, 450, 555, 680, and/or 814 nm, including some ground based images to complement filters missing with HST. These nearby galaxies are all large enough that a ground-based V-band image yields the same classification as an HST F555W or F606W image. These authors conclude that the change in rest-frame morphology going from the red to the mid-far UV is more pronounced for early type galaxies (as defined at the traditional optical wavelengths or V-band), but not necessarily negligible for all mid-type spirals or star-forming galaxies. Late-type galaxies generally look more similar in morphology from the mid-UV to the red due to their more uniform and pervasive SF that shows similar structure for young-old stars in all filters from the mid-UV through the red. Wind-

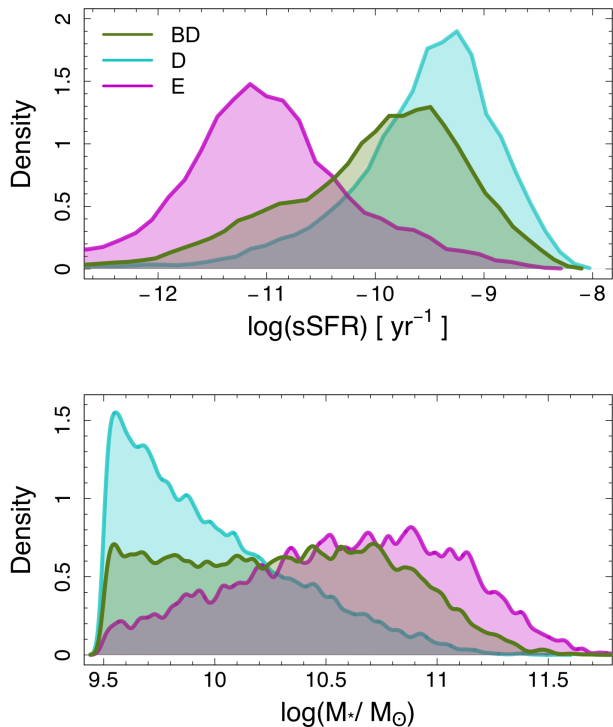


Figure 7. Top panel: the PDF of the specific star formation rate ($\text{sSFR} = \text{SFR}/M_*$) of the same morphologies. Bottom panel: the stellar mass probability density function (PDF) of three morphologies in our sample (all redshifts), i.e. *pure-disk* (cyan), *double-component* (green) and *elliptical* (magenta) galaxies. Note that for clarity, the PDFs are slightly smoothed by a kernel with standard deviation of 0.02.

horst et al. (2002) conclude *qualitatively* that in the rest-frame mid-UV, early- to mid-type galaxies are more likely to be misclassified as later types than late-type galaxies are likely to be misclassified as earlier types.

To *quantify* these earlier qualitative findings regarding the morphological K-correction, much larger sample of 199 nearby galaxies across all Hubble types (as defined in V-band) was observed by Taylor et al. (2005) and Taylor-Mager et al. (2007), and 2071 nearby galaxies were similarly analyzed by Mager et al. (2018). They determined their SB-profiles, radial light-profiles, color gradients, and CAS parameters (Concentration index, Asymmetry, and Clumpiness; e.g. Conselice 2004) as a function of rest-frame wavelength from 150–823 nm.

Taylor-Mager et al. (2007) and Mager et al. (2018) conclude that early-type galaxies (E–S0) have CAS parameters that appear, within their errors, to be similar at all wavelengths longwards of the Balmer break, but that in the far-UV, E–S0 galaxies have concentrations and asymmetries that more closely resemble those of spiral and peculiar/merging galaxies in the optical. This may be explained by extended disks containing recent star formation. The CAS parameters for galaxy types later than S0 show a mild but significant wavelength dependence, even over the wavelength range 436–823 nm, and a little more significantly so for the earlier spiral galaxy types (Sa–Sc). These galaxies

Table 3. Final number of objects in each of our morphological classes.

Morphology	Object Number	Percentage
Double	15,931	44.4%
Pure Disk	13,212	37%
Elliptical	3,890	11%
Compact	1,124	3.1%
Hard	1,600	4.5%

generally become less concentrated and more asymmetric and somewhat more clumpy towards shorter wavelengths. The same is true for mergers when they progress from pre-merger via major-merger to merger-remnant stages.

While these trends are mostly small and within the statistical error bars for most galaxy types from 436–823 nm, this is not the case for the Concentration index and Asymmetry of Sa–Sc galaxies. For these galaxies, the Concentration index decreases and the Asymmetry increases going from 823 nm to 436 nm (Fig. 17 of Taylor-Mager et al. 2007 and Fig. 5 of Mager et al. 2018). Hence, to the extent that our visual classifications of apparent Sa–Sc galaxies depended on their Concentration index and Asymmetry, it is possible that some of these objects may have been misclassified. E–S0 galaxies show no such trend in Concentration and Clumpiness parameters generally much lower than Sa–Sc galaxies. Hence, it is not likely that a significant fraction of E–S0 galaxies are misclassified as Sa–Sc galaxies at $z \lesssim 0.8$ in the 436–823 nm filters due to the Morphological K-correction.

Sd–Im galaxies show milder trends in their CAS parameters and in the same direction as the Sa–Sc galaxies. It is thus possible that a small fraction of Sa–Sc galaxies — if visually relying heavily on Concentration and Asymmetry index — may have been visually misclassified as Sd–Im galaxies, while a smaller fraction of Sd–Im galaxies may have been misclassified as Sa–Sc galaxies. The available data on the rest-frame wavelength dependence of the morphology of nearby galaxies does not currently permit us to make more precise statements. In any case, these CAS trends with restframe wavelengths as observed at 436–823 nm for redshifts $z \simeq 0.8$ –0 in the F814W filter are shallow enough that the fraction of misclassifications between Sa–Sc and Sd–Im galaxies, and vice versa, is likely small.

2.5 Review

In Figure 4, we show the associated fractions of our final visual inspection as solid lines. The global trends are in good agreement with our initial 4k gold calibration sample. We find that, although our inspection procedure may have slightly changed from the 4k gold calibration sample to the full sample, the outcome classifications are consistent in the three primary classes making up more than 92% of our sample.

Figure 7 shows the probability density function (PDF) of the sSFR (upper panel) and total stellar mass (lower panel) for galaxies classified as D, BD and E. We use the

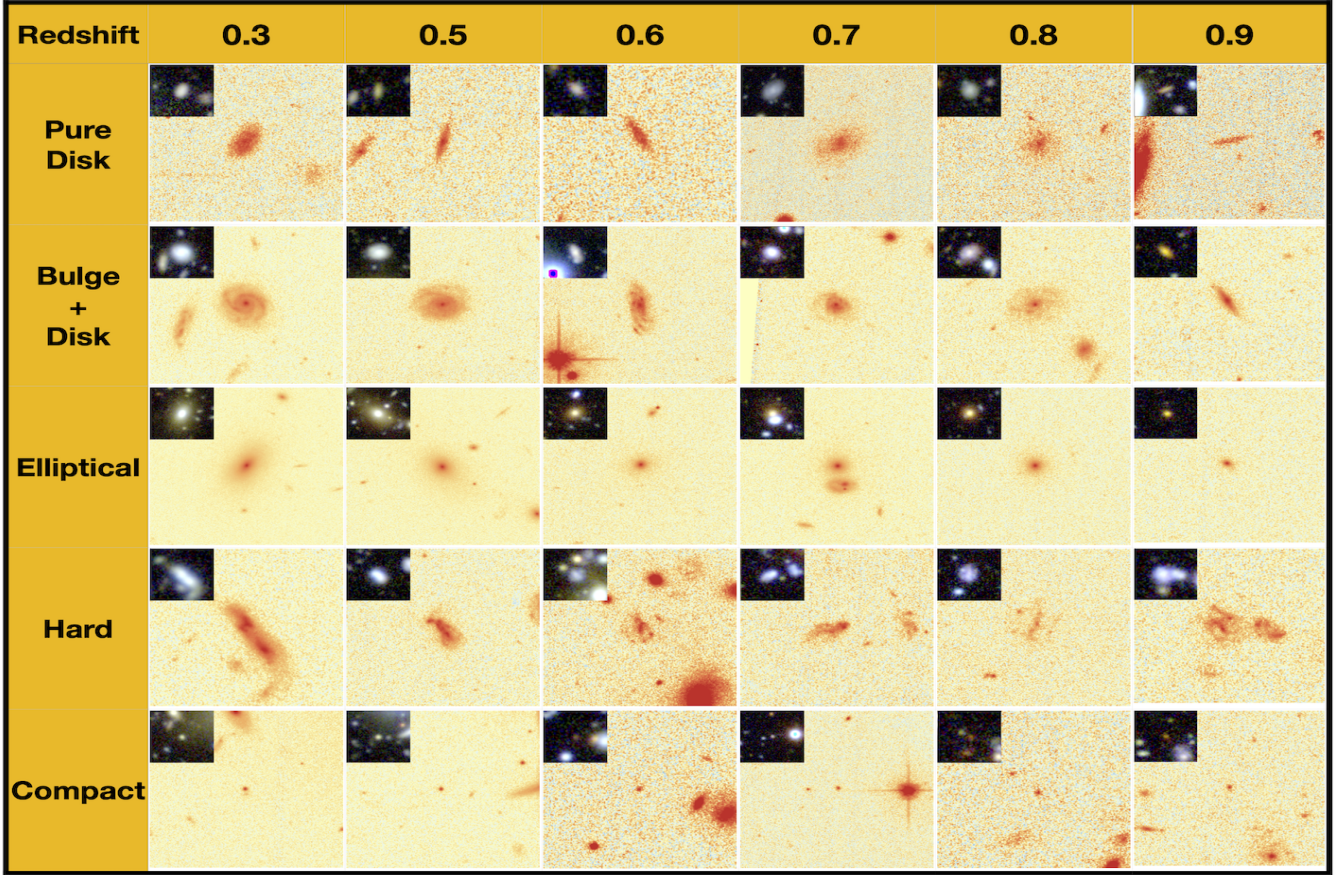


Figure 8. Random postage stamps of various morphologies that we generate to perform our visual inspection. Background images are HST ACS/F814W while insets are combined SUBARU *gri* colour image. Rows represent different morphologies. Galaxies are randomly selected within different redshift bins shown in columns. Redshifts annotated in the first row are the mean of the associated redshift bins. Cutouts indicate $5 \times R90$ on each side, where $R90$ is measured from UltraVISTA Y-band in the DEVILS photometry catalogue (Davies et al. in prep.).

SFR from the PROSPECT SED fits described in [Thorne et al. \(2020\)](#). These figures indicate that, as one would expect, D galaxies dominate lower stellar mass and higher sSFR regime, opposite to Es which occupy the high stellar mass end and low sSFR. BD galaxies are systems located in-between these two classes in terms of both stellar mass and sSFR. These results are as expected and provide some confidence that our classifications are sensible.

Figure 8 displays a set of random galaxies in each of the morphological classes within different redshift intervals. In addition, we present 50 random galaxies of each morphology in Figures 17–21.

Having finalised our morphological classification, we now investigate the stellar mass functions for different morphologies and their evolution from $z = 1$.

3 FITTING GALAXY STELLAR MASS FUNCTION

For parameterizing the SMF, we assume a fitting function that can describe the galaxy number density, $\Phi(M)$. The typical function adopted is that described by [Schechter \(1976\)](#) as:

$$\Phi(M)dM = \Phi^* e^{-M/M^*} \left(\frac{M}{M^*} \right)^\alpha dM, \quad (2)$$

where the three key parameters of the function are, α , the power law slope or the slope of the low-mass end, Φ^* , the normalization, and, M^* , the characteristic mass (also known as the break mass or the knee of the Schechter function).

At very low redshifts a number of studies have argued that the shape of the SMF is better described by a double Schechter function ([Baldry et al. 2008](#); [Pozzetti et al. 2010](#); [Baldry et al. 2012](#)), i.e. a combination of two single Schechter functions, parameterized by a single break mass (M^*), and given by:

$$\Phi(M)dM = e^{-M/M^*} \left[\Phi_1^* \left(\frac{M}{M^*} \right)^{\alpha_1} + \Phi_2^* \left(\frac{M}{M^*} \right)^{\alpha_2} \right] \frac{dM}{M^*}, \quad (3)$$

where $\alpha_2 < \alpha_1$, indicating that the second term predominantly drives the lower stellar mass range.

To fit our SMFs, we use a modified maximum likelihood (MML) method (i.e., not $1/V_{\max}$) as implemented

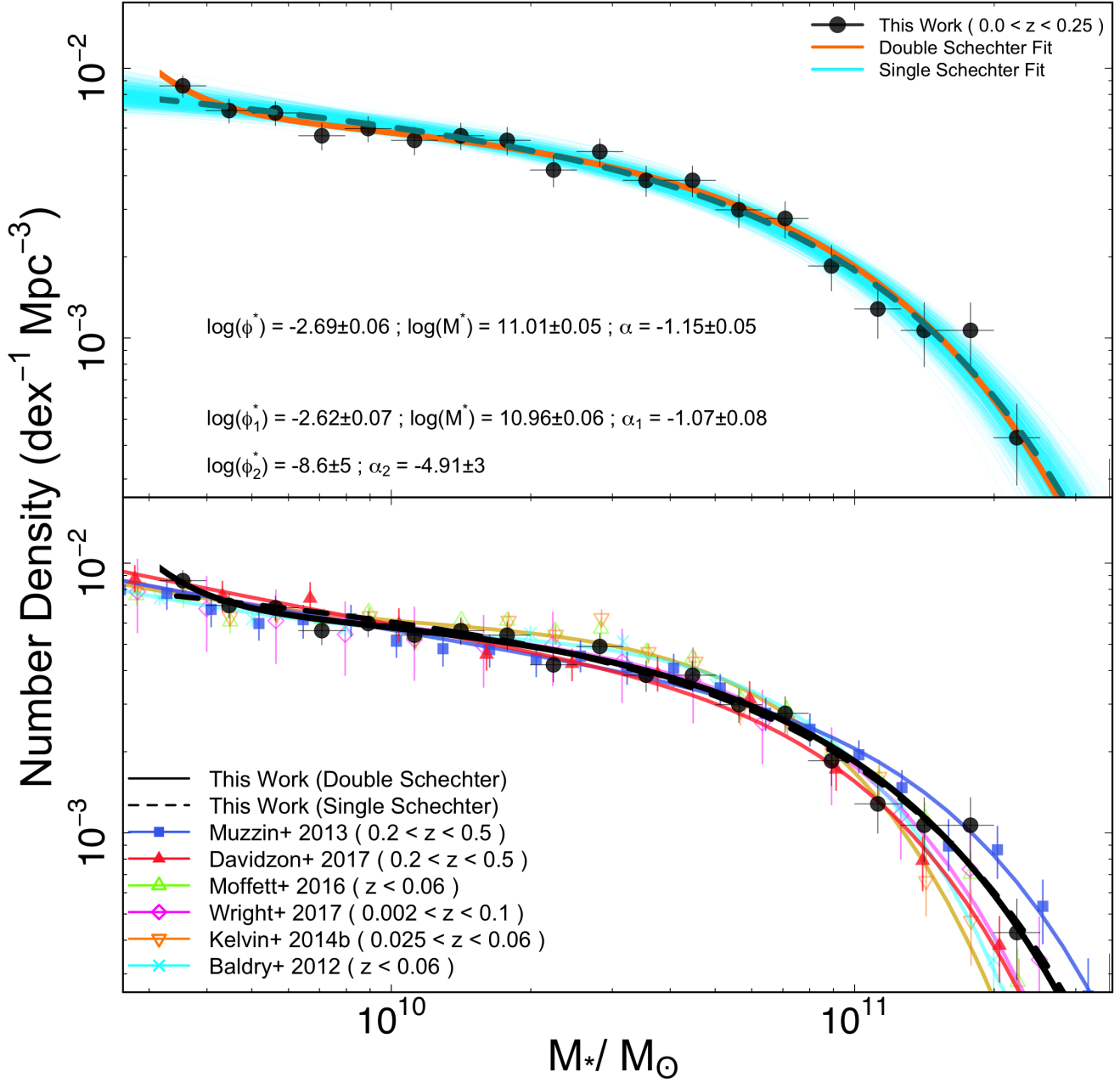


Figure 9. Top panel: Single and double Schechter functions fitted to a low- z sample of D10/ACS ($0.0 < z < 0.25$). The fits are performed by using `dftools` down to the stellar mass limit of the sample, i.e. $10^{9.5} M_\odot$. Transparent region shows the error range calculated by 1000 times sampling of the full posterior probability distribution of the single Schechter fit parameters. Black data points show the binned galaxy counts for which the stellar mass range from minimum to maximum ($9.5 \leq \log(M_*/M_\odot) \leq 12$) is binned into 25 equal-sized bins. Note that the Schechter functions are not fitted directly to the galaxy counts. Bottom panel: Comparison of our SMF at $0.0 < z < 0.25$ with Muzzin et al. (2013) and Davidzon et al. (2017). For completeness, the SMF of the GAMA local galaxies from several studies are shown in different colours. Solid and dashed black lines represent the double and single Schechter function fits to our data, respectively (eq. 2 & 3). Note that, the fits to other studies (colour solid lines) are double Schechter fits.

in `dftools`⁴ (Obreschkow et al. 2018). This technique has multiple advantages including: it is free of binning, accounts

for small statistics and Eddington bias. `dftools` recovers the mass function (MF) while simultaneously handling any complex selection function, Eddington bias and the cosmic large-scale structure (LSS). Eddington bias tends to change the distribution of galaxies, particularly in the low-mass

⁴ <https://github.com/obreschkow/dftools>

regime which is more sensitive to the survey depth and S/N, as well as high-mass regime due to the exponential cut-off which is sensitive to the scatters by noise (e.g. Ilbert et al. 2013; Caputi et al. 2015). Eddington bias occurs because of the observational/photometric errors and often can dominate over the shot noise (Obreschkow et al. 2018). Photometric uncertainties, which are introduced in the redshift estimation, as well as the stellar mass measurements are fundamentally the source of this bias (Davidzon et al. 2017). We account for Eddington bias in `dftools` by providing the errors on the stellar masses from the PROSPECT analysis by Thorne et al. (2020).

The R language implementation and MML method make `dftools` very fast. In the fitting procedures described in this work, we use the inbuilt `optim` function with the default optimization algorithm of Nelder & Mead (1965) for maximizing the likelihood function. In order to account for the volume corrections, we use the effective unmasked area of the D10/ACS region which we calculate to be 1.3467 square degrees. This is exclusive of the masked areas from bright stars and the non-uniform edges of the ACS mosaic (see Figure 1) and this is calculated using the process outlined in Davies et al. (in prep.). Our selection function, required for a proper volume corrected distribution function, is essentially a volume limited sample, i.e. a constant volume across adopted mass range. We refer the reader to Obreschkow et al. (2018) for full details regarding `dftools` and its methodology. In this paper, we fit both single and double Schechter functions to the SMF. We examine both functions and will discuss further in Section 3.1.

3.1 Verification of our SMF fitting process at low redshift

We first validate our *total* SMF fitting process at low- z and compare with the known literature, prior to splitting by redshift and morphology.

To achieve this, we compare the SMF of D10/ACS galaxies in our lowest- z bin, i.e. $0 < z < 0.25$, with literature studies. We primarily choose this redshift range to compare with the SMF Muzzin et al. (2013) and Davidzon et al. (2017) at $0.2 < z < 0.5$ in the COSMOS/UltraVISTA field and local GAMA galaxies at $z < 0.06$ (Baldry et al. 2012; Kelvin et al. 2014; Moffett et al. 2016; Wright et al. 2017). We fit the SMF within this redshift range using both single and double Schechter functions (Equations 2 and 3, respectively). The upper panel of Figure 9, shows our single and double Schechter fit to this low- z sample. As annotated in the figure, we report the best fit single Schechter parameters of $\log(M^*/M_\odot) = 11.01 \pm 0.05$, $\alpha = -1.15 \pm 0.05$, $\log(\Phi^*) = -2.69 \pm 0.06$ and $\log(M^*/M_\odot) = 10.96 \pm 0.06$, $\alpha_1 = -1.07 \pm 0.08$, $\alpha_2 = -4.91 \pm 3$, $\log(\Phi_1^*) = -2.62 \pm 0.07$ and $\log(\Phi_2^*) = -8.6 \pm 5$ in our double Schechter fit. Therefore, the double Schechter fit involves a broad range of uncertainty, in particular at the low-mass range. Larger uncertainty is likely due to the fact that the stellar mass range of the D10/ACS sample does not extend to $\log(M_*/M_\odot) < 9.5$, where the pronounced upturn in the SMF occurs. The error ranges shown in the upper panel of Figure 9 as transparent curves are obtained from 1000 samples drawn from the full posterior probability distribution of all the single Schechter parameters.

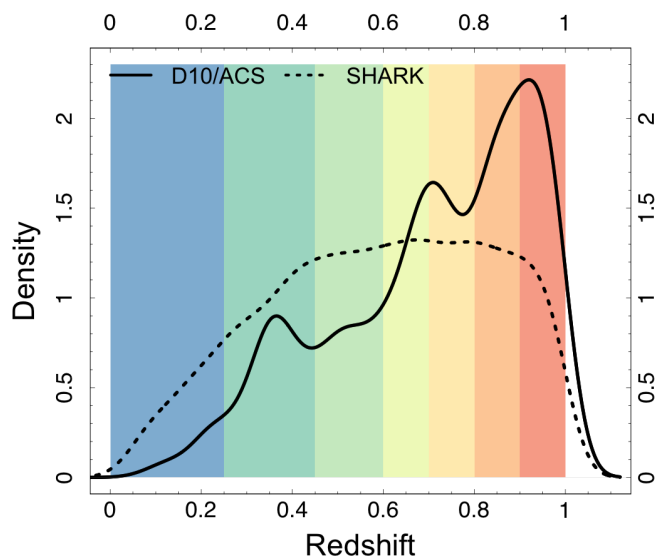


Figure 10. The $N(z)$ distribution of the D10/ACS sample (solid line) compared with the SHARK semi-analytic model prediction (dashed line). SHARK data represent a light-cone covering 107.889 square degrees with $Y\text{-mag} < 23.5$. Colour bands represent the redshift bins that we consider in this work. Note that the PDFs are smoothed by a kernel with standard deviation of 0.3 so are non-zero beyond the nominal limits.

Despite larger errors on the double Schechter parameters, we elect to use this function for our future analysis at all redshifts as it has been shown that a double Schechter can better describe the stellar mass distribution even at higher- z (e.g., Wright et al. 2018).

In the lower panel of Figure 9, we show that our SMF is in good agreement with Muzzin et al. (2013) and Davidzon et al. (2017) within the quoted errors. Overall, we see a good agreement with the mass function of galaxies at low- z . We observe no significant flattening of the SMF at the intermediate stellar masses ($10^{9.5} - 10^{10.5}$) as reported in the local Universe by e.g., Moffett et al. (2016). We are unsurprised that we do not see this flattening as the D10/ACS contains only 3 galaxies in the redshift range comparable to GAMA ($z < 0.06$).

One might expect an evolution of the SMF within $0 < z < 0.25$ that would explain the slightly higher number density in the intermediate mass range. Our fitted Schechter functions however also deviate from the GAMA SMFs in the high stellar mass end. We find that this is systematically due to the Schechter function fitting process. Unlike D10/ACS, as shown in Figure 9, the local literature data extend to lower stellar mass regimes ($\log(M_*/M_\odot) = 8$ and 7.5 in the case of Wright et al. 2017), influencing the bright end fit and the position of M^* . In this regime the upturn of the stellar mass distribution is remarkably more pronounced. This strong upturn drives the optimization fitting and impacts the high-mass end. This highlights the difficulty in directly comparing fitted Schechter values if fitted over different mass ranges.

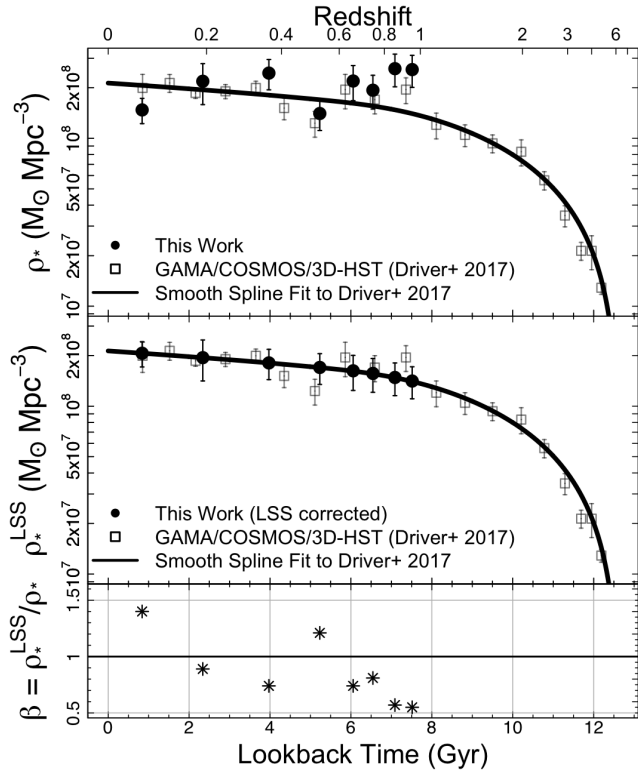


Figure 11. Top panel: our measurement of the evolution of the *total* SMD (per comoving Mpc^3) compared with a compilation of GAMA, COSMOS and 3D-HST by [Driver et al. \(2018\)](#). The black curve represents a spline fit to the [Driver et al. \(2018\)](#) data. Middle panel: the large scale structure correction factor applied to our SMD in order to meet the predictions of the spline fit. Bottom panel: the residual of the SMDs before and after the LSS correction indicating the correction coefficient we apply to each redshift bin.

3.2 Cosmic Large Scale Structure Correction

All galaxy surveys are to some extent influenced by the cosmic large scale structure (LSS, [Obreschkow et al. 2018](#)). Generally, the LSS produces local over- and under-densities of the galaxies at particular redshifts in comparison to the mean density of the Universe at that epoch. For example, GAMA regions are $\sim 10\%$ underdense compared with SDSS ([Driver et al. 2011](#)).

We observe this phenomenon in the nonuniform D10/ACS redshift distribution, $N(z)$. To highlight this, Figure 10 compares the $N(z)$ distribution of the D10/ACS sample with the prediction of the SHARK semi-analytic model ([Lagos et al. 2018; Lagos et al. 2019](#)). SHARK data in this figure represent a light-cone covering 107.889 square degrees with $Y\text{-mag} < 23.5$, and because of the much larger simulated volume, is less susceptible to LSS. In this figure the redshift bins we shall use later in our analysis are shown as background colour bands indicating redshift intervals of (0, 0.25, 0.45, 0.6, 0.7, 0.8, 0.9 and 1.0). SHARK predicts a nearly uniform galaxy distribution with no significant over- and under-density regions, while the empirical D10/ACS sample shows a nonuniform $N(z)$ with overdensities and under-densities. These density fluctuations can introduce system-

atic errors in the construction of the SMF by, for example, overestimating the number density of very low-mass galaxies which are only detectable at lower redshifts ([Obreschkow et al. 2018](#)). In other words, the LSS can artificially change the shape/normalization of the SMF.

Using the distance distribution of galaxies, `dftools` ([Obreschkow et al. 2018](#)) internally accounts for the LSS by modeling the relative density in the survey volume, $g(r)$, i.e. it measures the mean galaxy density of the survey at the comoving distance r , relative to the mean density of the Universe. Incorporating this modification into the effective volume, the MML formalism works well for a sensitivity-limited sample (see [Obreschkow et al. 2018](#) for details). However, for our volume limited sample, this method is unable to thoroughly model the density fluctuations. Therefore, to take this non-uniformity into account, we perform a manual correction as follows.

In a comprehensive study of the cosmic star formation history, [Driver et al. \(2018\)](#) compiled GAMA, COSMOS and 3D-HST data to estimate the total stellar mass density from high redshifts to the local Universe ($0 < z < 5$). Figure 11 (upper panel) shows these data. As we know the total stellar mass density must grow smoothly and hence we assume that perturbations around a smooth fit represent the underlying LSS. In Figure 11 (middle panel), we fit a smooth spline with the degree of freedom 3.5 to the [Driver et al. \(2018\)](#) data to determine a uniform evolution of the total ρ_* . We then introduce a set of correction factors (β) to our empirical measurements of the *total* SMDs to match the prediction of the spline fit (middle panel of Figure 11). We then apply these correction factors (bottom panel of Figure 11) to our estimations of the morphological SMD values. This ignores any coupling between morphology and LSS which we consider a second order effect. We report the β correction factors in Table 4 and show them in the bottom panel of Figure 11.

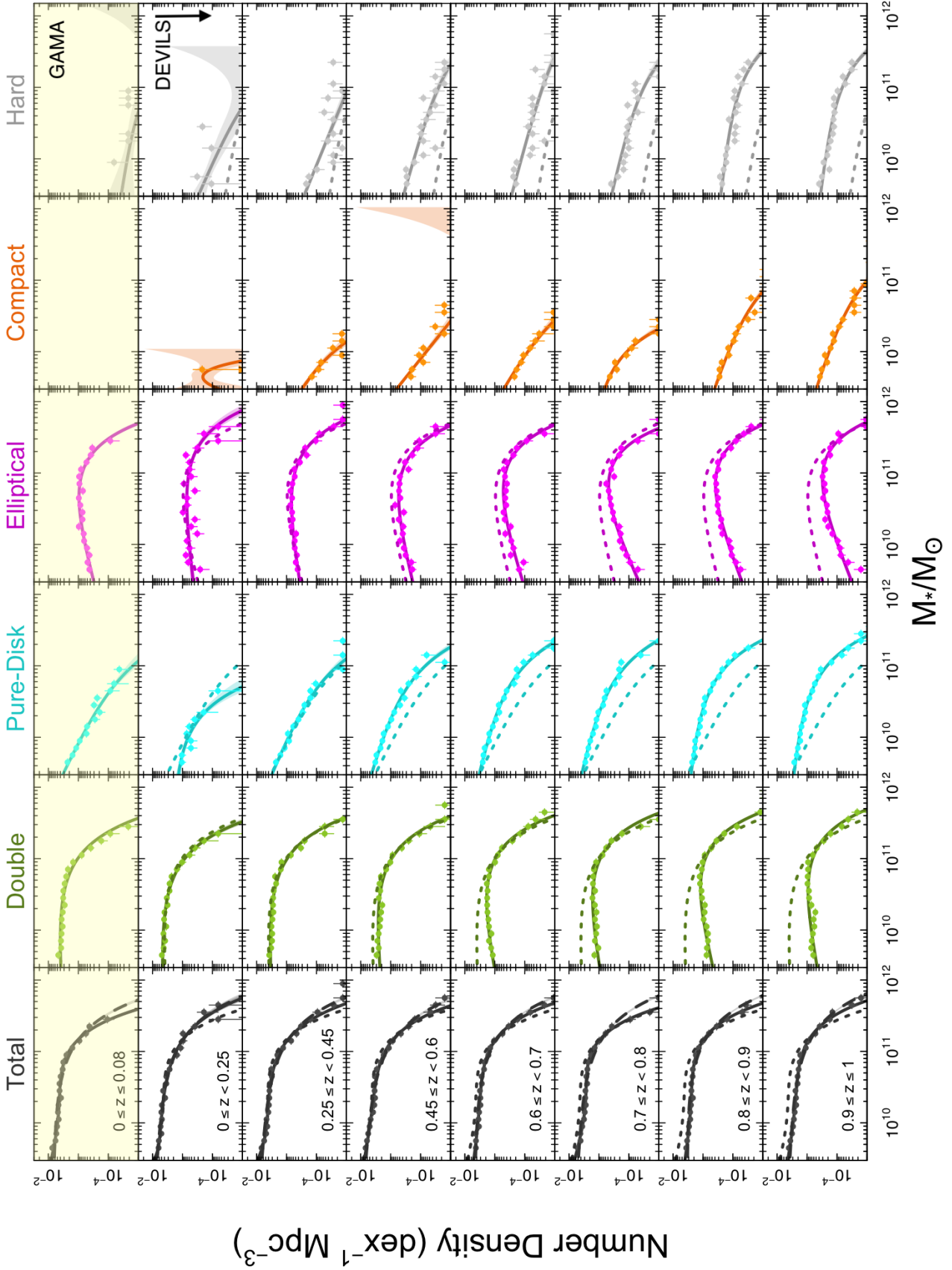


Figure 12. The *total* and morphological SMFs in eight redshift bins. Top row highlighted by yellow colour represents the GAMA SMFs ($0 \leq z \leq 0.08$). Data points are galaxy counts in each of equal-size stellar mass bins. Width of stellar mass bins are shown as horizontal bars on data points. Vertical bars are poisson errors. Shaded regions around the best fit curves are 68 per cent confidence regions. Black solid and dashed curves demonstrate double and single Schechter functions of all galaxies, respectively, while dotted curves over-plotted on higher- z bins are the GAMA $z = 0$ SMFs to highlight the evolution of the SMF.

3.3 Evolution of the SMF since $z = 1$

With the LSS correction in place, we now split the sample into 7 bins of redshift (0-0.25, 0.25-0.45, 0.45-0.6, 0.6-0.7, 0.7-0.8, 0.8-0.9 and 0.9-1.0) so that we have enough numbers of objects in each bin and are not too wide to incorporate a significant evolution (these redshift ranges are shown by the colour bands in Figure 10). Each bin contain 1,108, 5,041, 4,216, 4,867, 5,277, 7,090, 8,207 galaxies, respectively.

Figure 12 shows the SMF in each redshift bin for the full sample, as well as for different morphological types of: *double-component* (BD), *pure-disk* (D), *elliptical* (E), *compact* (C) and *hard* (H). These SMF measurements include the correction for LSS as discussed in Section 3.2. Note that the first row of Figure 12 highlighted by yellow shade shows GAMA $z = 0$ SMFs (Driver et al., in prep.).

As shown in Figure 12, we fit the *total* SMF within all 8 redshift bins (including GAMA) by both single and double Schechter functions (displayed as dashed and solid black curves, respectively), while the morphological SMFs are well fit by single Schechter function at all epochs. The difference between double and single Schechter fits is insignificant, compared to the error on individual points. However, as noted in Section 3.1, for calculating the stellar mass density we will use our double Schechter fits. As we will see later, the effect of this choice on the measurement of our total stellar mass density is negligible. In Figure 12, we over-plot the GAMA $z = 0$ SMFs (Driver et al., in prep.) on higher- z to highlight the evolution (dotted curves). In the *total* SMF we see a growth at the low-mass end and a relative stability at high-mass end, particularly when comparing high- z with the D10/ACS low- z ($0 < z < 0.25$). At face value, this suggests that since $z = 1$ in-situ star formation and minor mergers (low-mass end) play an important role in forming or transforming mass within galaxies (Robotham et al. 2014).

Looking at the SMF of the morphological sub-classes we find that the BD systems show no significant growth with time at their high-mass end, while at the low-mass end we see a noticeable increase in number density. In D galaxies, at both low- and high-mass ends we find a variation in the number density with the low-mass end increasing and extreme steepening at the lower- z and high-mass end decreasing with time. Note that we do not rule out the possible effects of some degree of incompleteness in this mass regime on the evolution of the low-mass end. For E galaxies, however, we report a modest growth in their high-mass end (again when comparing with D10/ACS low- z) and a significant growth in intermediate- and low-mass regimes from $z = 1$ to $z = 0$. Finally, H and C systems become less prominent with declining redshift as fewer galaxies occupy these classes. The physical implications of these trends will be discussed in Section 5.

Figure 13 further summarizes the trends in Figure 12, showing the evolution of our best fit single Schechter parameters Φ^* , M^* and α . We report the best Schechter fit parameters in Table 6. For comparison, we also show a compilation of literature values in the right panel. The literature data show only single Schechter parameters of the *total* SMF. Comparing our *total* SMF with other studies, including Muzzin et al. (2013), we find a good agreement within the quoted errors.

Note that the three parameters are, of course, highly correlated and the mass limits to which they are fitted vary.

The Φ^* of BD systems has the largest value and almost mimics the trend of the *total* Φ^* which is largely consistent with no evolution. This is expected as BD galaxies dominate the sample at almost all redshifts. We report a slight decrease in the Φ^* value of D galaxies, while almost no evolution in E systems. Note that as mentioned earlier, our lowest redshift bin ($0.0 < z < 0.25$) contains only 1,108 galaxies of which only 102 are D systems incorporating an uncertainty in our fitting process. This can be seen in the deviation of the second data point of D galaxies (cyan lines) from other redshifts in Figure 13. H systems also contribute more at higher redshifts (higher Φ^* values) owing to the fact that the abundance of mergers, clumpy and disrupted systems dramatically increases at higher redshifts (despite lower resolution). We note that due to our LSS corrections (Section 3.2) the Φ^* reported here is not the directly measured parameter but modified according to our LSS correction coefficients (reported in Table 4). This normalization smooths out the evolutionary trends, otherwise fluctuating due to the large scale structures, but does not impact their global trends.

The characteristic mass, M^* , of the BD systems presents a stable trend since $z = 1$. We interpret this behaviour to be a result of the lack of significant evolution of the massive/intermediate-mass regime of the SMF of this morphological class. D galaxies also show slight evidence of evolution with some fluctuations in M^* value. E galaxies, likewise, evolve only a small amount. Overall, we observe a behaviour consistent with no evolution in M^* for all morphological types. Note that large variation of the M^* in H and C types, at low- z in particular, is not physical. This is massively driven by the lack of H and C galaxies at low- z resulting in an unconstrained turnover and as can be seen in Figure 13 large uncertainties.

The low-mass end slope, α , of different morphological classes also shows some evolution. Similar to D systems, BD galaxies show a marked steepening increase in their slope at later times, indicating that the SMF steepens at lower redshifts. The steepest mass function at almost all times is for the D galaxies. E galaxies occupy the lowest steepening but constantly growing from $\alpha = 0.34$ to -0.75 at $z \sim 0.2$.

4 THE EVOLUTION OF THE STELLAR MASS DENSITY SINCE $z = 1$

In this section, we investigate the evolution of the Stellar Mass Density (SMD) as a function of morphological types. To determine the SMD, we integrate under the best fit Schechter functions over all stellar masses from $10^{9.5}$ to ∞ . This integral can be expressed as a gamma function:

$$\rho_* = \int_{M=10^{9.5}}^{\infty} M' \Phi(M') dM' = \Phi^* M^* \Gamma(\alpha + 2, 10^{9.5}/M^*), \quad (4)$$

where Φ^* , M^* and α are the best regressed Schechter parameters. Figure 14 shows the evolution of the distribution of the SMDs, term $M' \Phi(M')$, for different morphologies. We also illustrate the fitting errors by sampling 1000 times the full posterior probability distribution of the fit parameters. These are shown in Figure 14 as transparent shaded regions around the best fit curves. The standard deviations of the

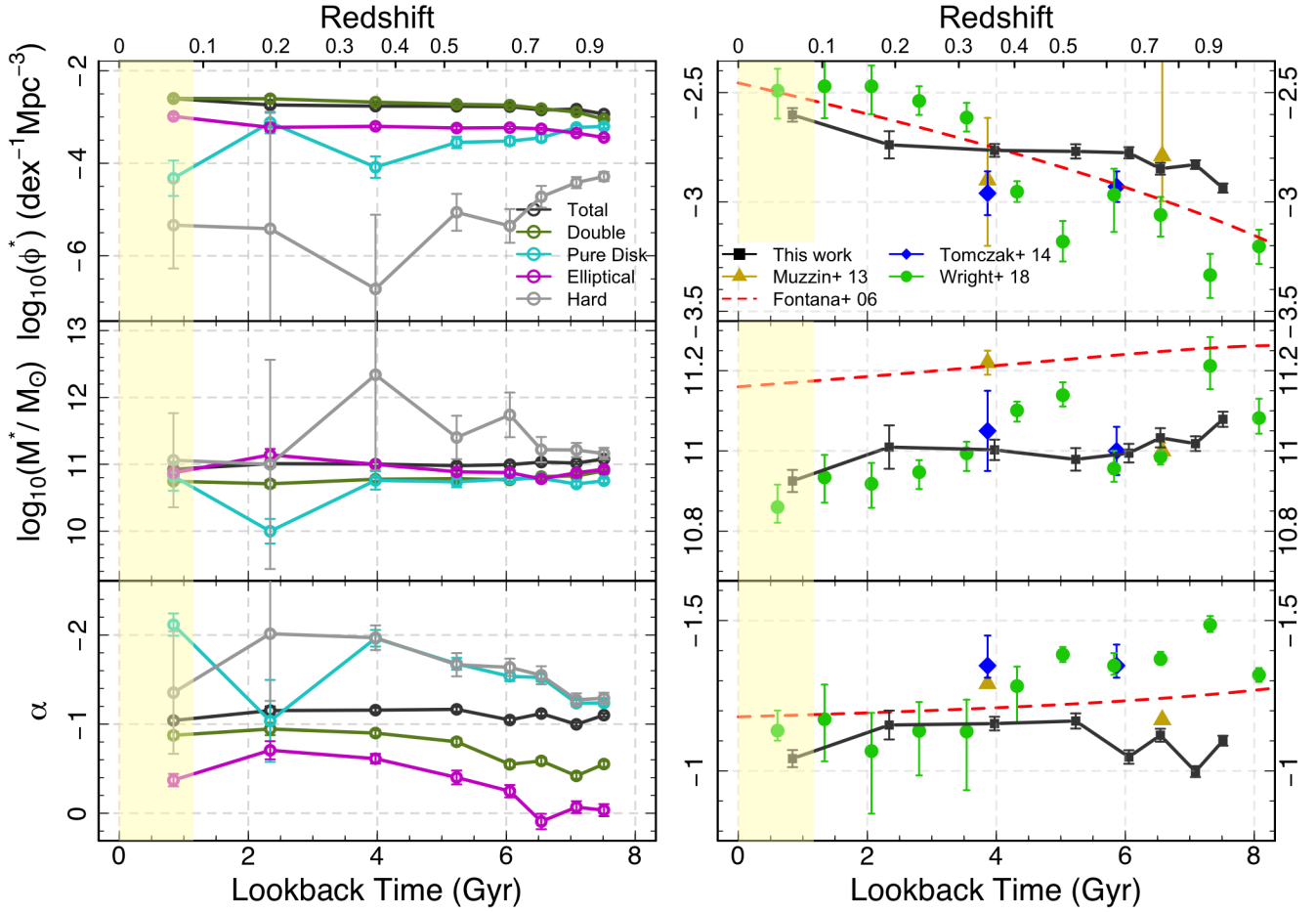


Figure 13. Left: Evolution of the single Schechter best fit parameters, Φ^* , M^* and α . Error bars are the standard deviations on each of the most likely parameters. Black line is the *total* SMF while colour coded data represent the best fit parameters of the Schechter function of different morphologies. Note that for simplicity we remove *compacts* as their trends are very noisy and washes out the trends of other morphological types. Right: Zoomed-in plot showing the evolution of our *total* Schechter function parameters compared with a compilation of other studies. Highlighted region shows the epoch covered by the GAMA data.

integrated SMD calculated from each of these functions are reported as the fit error on ρ_* in Table 4. As can be seen in Figure 14, the distribution of the stellar mass density of all individual morphological types in almost all redshift bins is captured, implying that integrating under these curves will capture the majority of the stellar mass for each class.

Figure 15 then shows the evolution of the integrated SMD, ρ_* , in the Universe between $z = 0 - 1$. This includes the LSS correction by forcing our *total* SMD values to match the smooth spline fit to the Driver et al. (2018) data, as described in Section 3.2. The uncorrected evolutionary path of ρ_* is shown in the upper panel of Figure 11.

We report the empirical LSS corrected ρ_* values in Table 4. This table also provides the LSS correction factor, β , so one might obtain the original values by $\rho_*^{Orig} = \rho_*^{corr}/\beta$.

For completeness, we show the evolution of the SMDs before we apply the LSS corrections in Figure 22 of Appendix 11. In this Figure, the trends are not as smooth as one would expect without the LSS correction being applied, given the evident structure in the $N(z)$ distribution from Figure 10. However, even without the LSS corrections, the main trends are still present, albeit not as strong. This high-

lights that the LSS correction is an important aspect and also the need for much wider deep coverage than that currently provided by HST. This will become possible in the coming Euclid and Roman era.

Before we analyse the evolution of the SMDs in Figure 15, below we investigate the errors that are involved in this calculation.

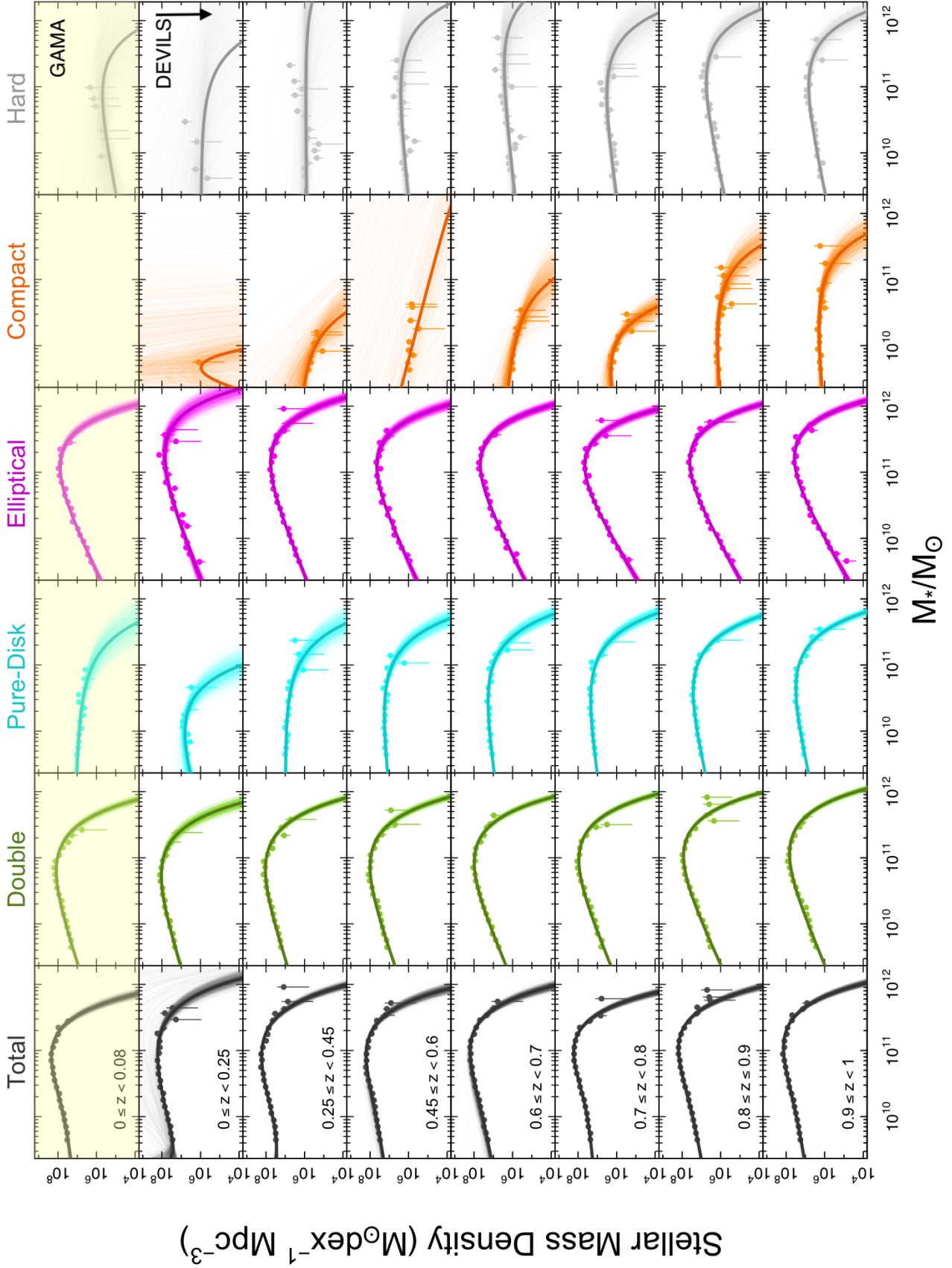


Figure 14. The distribution of *total* and morphological stellar mass density in different redshifts. Redshift bins are the same as Figure 12. Points and lines indicate $M^*\Phi(M')$ in Equation 4, where $\Phi(M')$ is our Schechter function fit. The shaded transparent regions represent the error range calculated by 1000 times sampling of the full posterior probability distribution of the fit parameters. The distribution of the stellar mass density of all individual morphological types in almost all redshift bins is bounded. Top row highlighted by yellow colour represents the GAMA data ($0 \leq z \leq 0.08$).

4.1 Analysing the Error Budget on the SMD

The error budget on our analysis of the SMD includes *cosmic variance* (CV), *fit error*, *classification error* and *Poisson error*. Cosmic variance and classification are the dominant sources of error.

We make use of Driver & Robotham (2010) equation 3 to calculate the *cosmic variance* in the volume encompassed within each redshift bin. This calculation is implemented in the R package: *celestial*⁵. Note that for our low- z GAMA data, instead of using Driver & Robotham (2010) equation that estimates a $\sim 22.8\%$ cosmic variance, we empirically calculate the CV using the variation of the SMD between 3 different GAMA regions of G09, G12, and G15 with a total effective area of 169.3 square degrees (G09:54.93; G12: 57.44; G15: 56.93, Bellstedt et al. 2020) and find CV to be $\sim 16\%$.

We measure the *fit error* by 1000 times sampling of the full posterior probability distribution of the Schechter parameters (shown as shaded error regions in Figure 14) and calculating the associated ρ_* in each iteration. We calculate the *classification error* by measuring the stellar mass density associated with each of our 3 independent morphological classifications. The range of variation of the SMD between classifiers gives the error of our classification. The *Poisson error* is calculated by using the number of objects in each morphology per redshift bin.

The combination of all the above error sources will provide us with the total error that is reported in Table 4.

As can be seen in Figure 15, the extrapolation of our D10/ACS ρ_* to $z = 0$ agrees well with the our local GAMA estimations. Note slight difference in D, but consistent in errors.

The total change in the stellar mass is consistent with observed SFR evolution (e.g., Madau & Dickinson 2014; Driver et al. 2018) as we will discuss more in Section 5. Analysing the evolution of the SMD (Figure 15), we find that in total (black symbols), 68% of the current stellar mass in galaxies was in place ~ 8 Gyr ago ($z \sim 1.0$). The top panel of Figure 16 illustrates the variation of the ρ_* ($\rho_z^*/\rho_{z=0}^*$), where ρ_z^* is the SMD at redshift z while $\rho_{z=0}^*$ represents the final SMD at $z = 0$.

According to our visual inspections C types are closer to Es than other subcategories. We, therefore, combine C types with E galaxies that shows a smooth growth with time of a factor of ~ 2.5 up to $z = 0.25$ and flattens out since then ($0.0 < z < 0.25$). Note that as reported in Table 4 the amount of mass in the C class is very little. This demonstrates a significant mass build-up in E galaxies over this epoch ($\sim 150\%$). We also note that the large error bars on some of E+C data points are dominantly driven by the large errors in C SMDs.

Having analytically integrated the SMD, we now measure the fraction of baryons in the form of stars ($f_s = \Omega_*/\Omega_b$) locked in each of our morphological types. We adopt $\Omega_b = 0.0493$ as estimated from Planck by Planck Collaboration et al. (2020) and the critical density of the Uni-

verse at the median redshift of GAMA, i.e. $z = 0.06$ to be $\rho_c = 1.21 \times 10^{11} \text{M}_\odot \text{Mpc}^{-3}$ in a 737 cosmology.

As shown in the bottom panel of Figure 16, at our D10/ACS lowest redshift bin $\bar{z} \sim 0.18$ we find the fraction of baryons in stars $f_s \sim 0.033 \pm 0.009$. Including our GAMA measurements at $\bar{z} \sim 0.06$ we find this fraction to be $f_s \sim 0.035 \pm 0.006$. As shown in Figure 16, this result is consistent with other studies within the quoted errors for example: Baldry et al. (2006), Baldry et al. (2012) and Moffett et al. (2016). The evolution of the fraction of baryons locked in stars, f_s , shows that it has increased from $(2.4 \pm 0.5)\%$ at $z \sim 1$ to $(3.5 \pm 0.6)\%$ at $z \sim 0$ indicating an increase of a factor of ~ 1.5 during last 8 Gyr.

Figure 16 also shows the breakdown of the total f_s to each of our morphological subcategories highlighting that as expected BD systems contribute the most to the stellar baryon fraction increasing from $f_s = 0.011 \pm 0.006$ to $f_s = 0.022 \pm 0.005$ at $0 < z < 1$. E+C systems take less percentage of the total f_s but increase their contribution from 0.005 ± 0.001 to 0.012 ± 0.002 while D galaxies decrease from $f_s = 0.006 \pm 0.002$ to $f_s = 0.001 \pm 0.005$ between $0 < z < 1$. We report our full f_s values for all morphological types at all redshifts in Table. 5.

In summary, over the last 8 Gyr, double component galaxies clearly dominate the overall stellar mass density of the Universe at all epochs. The second dominant system is E galaxies. However the extrapolation of the trends to higher redshifts in Figures 15 and 16 indicates that D systems are likely to dominate over Es in the very high- z regime ($z > 1$), which is reasonable according to the rise of the cosmic star formation history and the association of star-formation with disks.

5 DISCUSSION

Making use of our morphological classifications, we explore the evolution of the stellar mass function at $0 \leq z \leq 1$, to assess the physical processes that are likely affecting the individual morphological SMF. In particular, major mergers are thought to primarily occur between comparable mass companions (1:3) resulting in the fast growth of the SMF (Robotham et al. 2014). Conversely, secular activities, minor mergers and tidal interactions will primarily alter the number density at the low-stellar mass end of the SMF (Robotham et al. 2014). Investigating the *total* SMF (Figure 12) shows that unlike high-mass end the low-mass end grows significantly. This suggests that since $z \sim 1$, the galaxy population goes through mainly in-situ/secular processes at the low-mass end.

An important caveat, in what follows, is that although we have undertaken multiple tests of our visual classifications, possible uncertainties due to human classification error or inconsistencies will be present. Nevertheless some clear trends, which we believe are resilient to the classifications uncertainties are evident. Furthermore, we do not rule out the effects of dust in distinguishing bulges, particularly at high- z leading to overestimating the number of *pure-disk* systems at high redshifts. Although, high level of agreement in our visual classifications (see Figure 6) gives us some confidence that our evolutionary trends are unlikely dominated

⁵ The online version of this cosmology calculator is available at: <http://cosmocalc.icrar.org/>

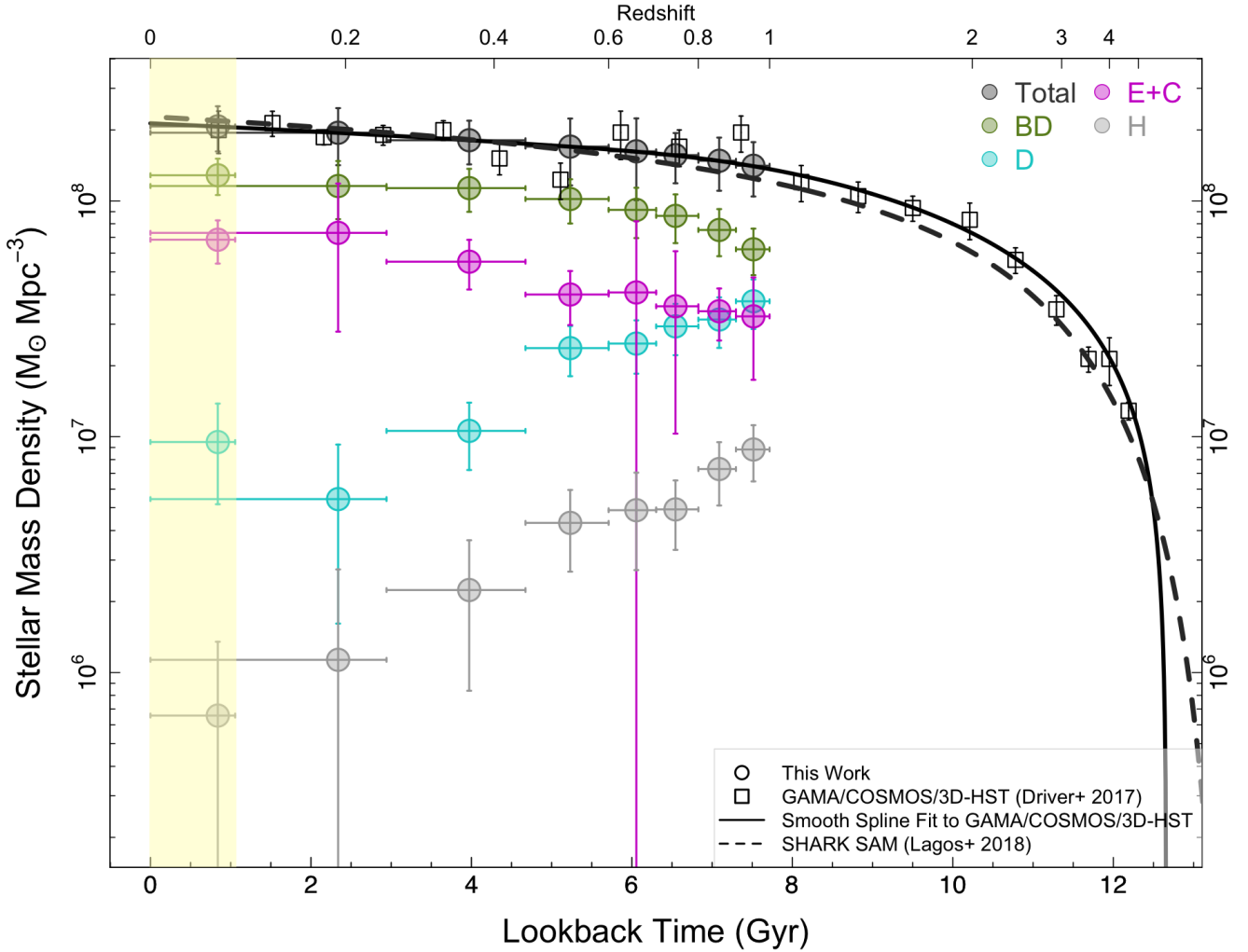


Figure 15. The evolution of the *total* and morphological stellar mass density, ρ_* , in the last 8 Gyr of the cosmic age. ρ_* expresses our measurements of the analytical integration under the best Schechter function fits in 8 redshift bins, i.e. Equation 4. Highlighted region shows the epoch covered by the GAMA data ($0 \leq z \leq 0.08$). This figure includes the correction for the large scale structure, LSS, that we apply by fitting a smooth spline to the empirical data of GAMA/G10COSMOS/3D-HST by Driver et al. (2018). See the text for more details on our method for this correction. The prediction of the SHARK semi-analytic model is also overlaid as dashed line. Colour codes are similar to Figure 12. Vertical bars on the points show the total error budget on each data point including: cosmic variance within the associated redshift bin taken from Driver & Robotham (2010), classification error, fit error and Poisson error. See Section 4.1 for more details about our error analysis. Horizontal bars indicate the redshift ranges while the data points are plotted at the mean redshift.

by incorrect classifications, it is possible that all classifiers agree on the incorrect classification.

Firstly, double component galaxies display a modest decrease with redshift in the high-stellar mass end of their SMF (Figure 12), whilst their low-stellar mass end steepens significantly. This could be interpreted as most of the stellar mass in double component systems evolving via lower mass weighted star formation or secular activity, rather than major merging, i.e., BD systems are not merging together to form higher-mass BD systems.

Secondly, *pure-disk* systems show a strong increase at the low-mass end and a *decrease* at their high-mass end. The low-mass end evolution suggests in-situ star formation of the disk and/or the formation of new disks. However, the decrease at the high-mass end is to some extent unphysical,

unless these systems are undergoing a transformation from the D class to another class. The most likely prospect is the secular formation of a central bulge component, resulting in a morphological transformation into the BD class. Hence, as time progresses and the second component forms, galaxies exit the D class leading to a mass-deficit at the high-mass end.

The new component forming through such an in-situ process is most likely a pseudo-bulge (pB), resulting in mass loss from the high-mass D SMF and a corresponding mass gain at comparable mass in the BD class.

Finally, *elliptical* galaxies, generally thought to be inert, show little growth in their high-mass end but a significant growth of low- and intermediate mass end presumably due to mergers.

Table 4. The *total* and morphological stellar mass density in different redshift ranges displayed in Figure 15 (left panel). ρ_* values are calculated from the integration under the best Schechter function fits. Note that the ρ_* are presented after applying the LSS correction. Columns represent: z -bin: redshift bins, \bar{z} : mean redshift, LBT: lookback time, T (S-Schechter): *total with single Schechter*, T (D-Schechter): *total with double Schechter*, BD: *bulge+disk*, pD: *pure-disk*, E: *elliptical*, C: *compact*, H: *hard*, β : the large scale structure correction factor. Errors incorporate all error sources including, cosmic variance, fit error, Poisson error and classification error (see Section 4.1 for details).

z -bin	\bar{z}	LBT (Gyr)	$\log_{10}(\rho_*/M_\odot)$							
			T (S-Schechter)	T (D-Schechter)	BD	pD	E	C	H	β
$0.00 \leq z < 0.08$	0.06	0.82	8.315 ± 0.08	8.316 ± 0.11	8.109 ± 0.08	6.977 ± 0.26	7.835 ± 0.10	–	5.818 ± 1.25	1.40
$0.00 \leq z < 0.25$	0.18	2.27	8.289 ± 0.14	8.289 ± 0.14	8.063 ± 0.14	6.735 ± 0.53	7.863 ± 0.20	5.332 ± 0.83	6.054 ± 0.38	0.89
$0.25 \leq z < 0.45$	0.36	3.95	8.258 ± 0.10	8.257 ± 0.10	8.054 ± 0.10	7.025 ± 0.17	7.740 ± 0.12	5.513 ± 1.23	6.350 ± 0.43	0.74
$0.45 \leq z < 0.60$	0.53	5.23	8.231 ± 0.10	8.230 ± 0.16	8.008 ± 0.10	7.376 ± 0.12	7.594 ± 0.13	5.936 ± 1.01	6.635 ± 0.21	1.21
$0.60 \leq z < 0.70$	0.65	6.05	8.210 ± 0.12	8.210 ± 0.21	7.962 ± 0.12	7.395 ± 0.13	7.603 ± 0.13	5.922 ± 0.60	6.688 ± 0.25	0.74
$0.70 \leq z < 0.80$	0.74	6.55	8.195 ± 0.11	8.194 ± 0.12	7.936 ± 0.12	7.468 ± 0.12	7.540 ± 0.13	6.032 ± 0.95	6.692 ± 0.17	0.81
$0.80 \leq z < 0.90$	0.85	7.07	8.171 ± 0.11	8.170 ± 0.13	7.877 ± 0.11	7.497 ± 0.12	7.508 ± 0.12	6.258 ± 0.55	6.863 ± 0.15	0.57
$0.90 \leq z \leq 1.00$	0.95	7.51	8.150 ± 0.11	8.149 ± 0.13	7.795 ± 0.11	7.574 ± 0.12	7.473 ± 0.12	6.430 ± 0.43	6.946 ± 0.14	0.55

The evolution of the global and morphological SMDs indicates that BD galaxies dominate ($\sim 60\%$ on average) the stellar mass density of the Universe since at least at $z < 1$. This morphological class also shows a constant mass growth, compared to other morphologies. As mentioned, D systems slightly decrease their stellar mass density with time. Presumably, the mass transfer out of the D class out-weighs the mass gain due to in-situ star-formation for this class.

We remark that the *rate* of mass growth in the BD systems also decreases with time. This is reflected in the decrease of their SMD slope although it is still steeper than the *total* SMD evolution and consistent with the general decline in the cosmic star-formation history. On the other hand, the E galaxies experience an initial growth until $z \sim 0.2$ and a recent flattening in their stellar-mass growth from $z = 1 - 0$ (see Figure 15 and the top panel of Figure 16).

6 SUMMARY AND CONCLUSIONS

We have presented a visual morphological classification of a sample of galaxies in the DEVILS/COSMOS survey with HST imaging, from the D10/ACS sample. The quality of the imaging data (HST/ACS) provides arguably the best current insight into galaxy structures and therefore the best pathway with which to explore morphological evolution.

We summarize our results as below:

- By visually inspecting galaxies out to $z \sim 1.5$, we find that morphological classification becomes far more challenging at $z > 1.0$ as many galaxies ($> 40\%$) no longer adhere to the classical notion of spheroids, bulge+disk or disk systems (Abraham & van den Bergh 2001). We see a dramatic increase in strongly disrupted systems, presumably due to interactions and gas clumps. Nevertheless, at all redshifts we find that more mass is involved in star-formation than in merging and most likely it is the high star-formation rates that are driving the irregular morphologies.
- The SMF of the D10/ACS sample in our lowest redshift bin ($z < 0.25$) is consistent with previous measurements from the local Universe.
- The evolution of the global SMF shows enhancement in both low- and slightly in high-mass ends. We interpret this

as suggesting that at least two evolutionary pathways are in play, and that both are significantly impacting the SMF.

- Despite a slight decrease in their high-mass end, BD systems demonstrate a non-negligible growth in the low-mass end of their SMF. In the D type, we witness a significant variation in both high- and low-mass ends of the SMF. We interpret the high-mass end decrease in D systems, which is at first sight unphysical, as an indication of significant secular mass transfer through the formation of pseudo-bulges and hence an apparent mass loss as galaxies transit to the BD category.

- E galaxies experience a modest growth in their high-mass end as well as an enhancement in their low/intermediate-mass end which we interpret as a consequence of major mergers resulting in the relentless stellar mass growth of this class.

- Despite the above shuffling of mass we find that the best regressed Schechter function parameters in the *total* SMF are observed to be relatively stable from $z = 1$. This is consistent with previous studies (Muzzin et al. 2013; Tomczak et al. 2014; Wright et al. 2018). Conversely, the component SMFs show significant evolution. This implication is that while stellar-mass growth is slowing, mass-transformation processes via merging and in-situ evolution are shuffling mass between types behind the scenes.

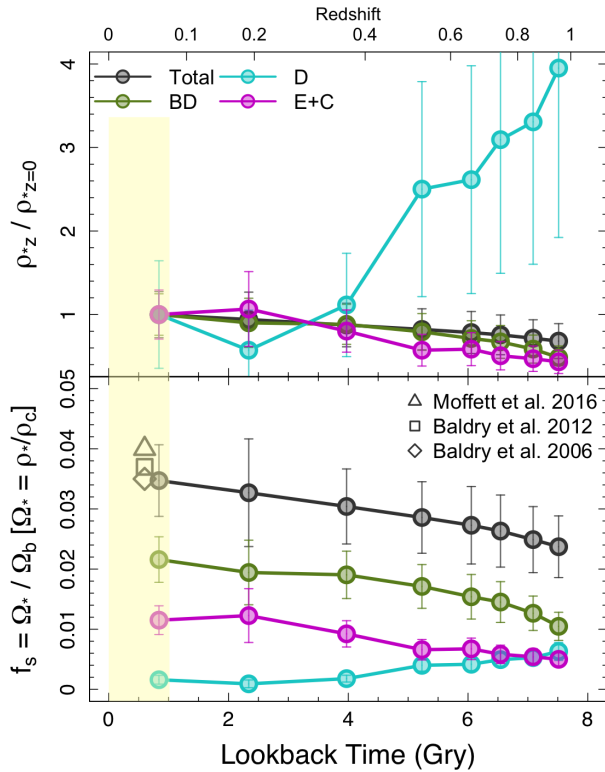
- We measured the integrated total stellar mass density and its evolution since $z = 1$ and find that approximately 32% of the current stellar mass in the galaxy population was formed during the last 8 Gyr.

- As shown in Figure 15, we find that the BD population dominates the SMD of the Universe within $0 \leq z \leq 1$ and has constantly grown by a factor of ~ 2 over this timeframe. On the other hand, the SMD of Ds declines slowly and eventually loses $\sim 85\%$ of its original value until $z \sim 0.2$. On the contrary, the E population experiences constant growth of a factor of ~ 2.5 since $z = 1$. We observe that the extrapolation of the trends of all of our morphological SMD estimations meets GAMA measurements at $z = 0$ (see Figure 15) except for the *pure-disk* systems which is likely due to unbound distribution of their SMD (see Figure 14).

One clear outcome of our analysis is that the late Uni-

Table 5. Total and morphological stellar baryon fraction (f_s) in different times. See the text for details.

Morphology Type	Redshift							
	$0.00 \leq z < 0.08$	$0.00 \leq z < 0.25$	$0.25 \leq z < 0.45$	$0.45 \leq z < 0.60$	$0.60 \leq z < 0.70$	$0.70 \leq z < 0.80$	$0.80 \leq z < 0.90$	$0.90 \leq z < 1.0$
Total	0.035 ± 0.006	0.033 ± 0.009	0.030 ± 0.006	0.029 ± 0.006	0.027 ± 0.006	0.026 ± 0.006	0.025 ± 0.005	0.024 ± 0.005
Double	0.022 ± 0.004	0.019 ± 0.005	0.019 ± 0.004	0.017 ± 0.004	0.015 ± 0.004	0.015 ± 0.003	0.013 ± 0.003	0.010 ± 0.002
Pure-Disk	0.002 ± 0.001	0.001 ± 0.001	0.002 ± 0.001	0.004 ± 0.001	0.004 ± 0.001	0.005 ± 0.001	0.005 ± 0.001	0.006 ± 0.001
Elliptical	0.012 ± 0.002	0.012 ± 0.004	0.009 ± 0.002	0.007 ± 0.002	0.007 ± 0.002	0.006 ± 0.002	0.005 ± 0.001	0.005 ± 0.001
Compact	—	0.000 ± 0.000	0.000 ± 0.000	0.000 ± 0.000	0.000 ± 0.000	0.000 ± 0.000	0.000 ± 0.000	0.000 ± 0.000
E+C	0.012 ± 0.002	0.012 ± 0.004	0.009 ± 0.002	0.007 ± 0.002	0.007 ± 0.002	0.006 ± 0.002	0.006 ± 0.001	0.005 ± 0.001
Hard	0.000 ± 0.000	0.000 ± 0.000	0.000 ± 0.000	0.001 ± 0.000	0.001 ± 0.000	0.001 ± 0.000	0.001 ± 0.000	0.001 ± 0.000

**Figure 16.** Top panel: the variation of the stellar mass density showing the fraction of final stellar mass density assembled or lost by each redshift, i.e. $\rho_{*z}/\rho_{*z=0}$. $\rho_{*z=0}$ is taken from GAMA estimations of the local Universe. Bottom panel: the evolution of the baryon fraction in form of stars (f_s). For simplicity, in this figure we only show the main morphological types and remove the *hard* and *compact* sub-classes. Highlighted region shows the epoch covered by the GAMA data.

verse ($z < 1$) appears to be a time of profound spheroid and bulge growth/emergence. To move forward and explore this further we conclude that to move forward it is key to decompose the double component morphological type, which significantly dominates the stellar mass density, into disks, classical bulges, and pseudo-bulges. To do this, requires robust structural decomposition which we will describe in Hashemizadeh et al. (in prep.) using our morphological classifications to guide the decomposition process.

7 ACKNOWLEDGEMENTS

DEVILS is an Australian project based around a spectroscopic campaign using the Anglo-Australian Telescope. The DEVILS input catalogue is generated from data taken as part of the ESO VISTA-VIDEO (Jarvis et al. 2013) and UltraVISTA (McCracken et al. 2012) surveys. DEVILS is part funded via Discovery Programs by the Australian Research Council and the participating institutions. The DEVILS website is <https://devilsurvey.org>. The DEVILS data is hosted and provided by AAO Data Central (<https://datacentral.org.au>). This work was supported by resources provided by The Pawsey Supercomputing Centre with funding from the Australian Government and the Government of Western Australia. We also gratefully acknowledge the contribution of the entire COSMOS collaboration consisting of more than 200 scientists. The HST COSMOS Treasury program was supported through NASA grant HST-GO-09822. SB and SPD acknowledge support by the Australian Research Council's funding scheme DP180103740. MS has been supported by the European Union's Horizon 2020 research and innovation programme under the Maria Skłodowska-Curie (grant agreement No 754510), the National Science Centre of Poland (grant UMO-2016/23/N/ST9/02963) and by the Spanish Ministry of Science and Innovation through Juan de la Cierva-formacion program (reference FJC2018-038792-I). ASGR and LJMD acknowledge support from the Australian Research Council's Future Fellowship scheme (FT200100375 and FT200100055, respectively).

This work was made possible by the free and open R software (R Core Team 2020). A number of figures in this paper were generated using the R *magicaxis* package (Robotham 2016b). This work also makes use of the *celestial* package (Robotham 2016a) and *dftools* (Obreschkow et al. 2018).

8 DATA AVAILABILITY

In this work, we draw upon two datasets; the established HST imaging of the COSMOS region (Scoville et al. 2007, Koekemoer et al. 2007), and multiple data products produced as part of the DEVILS survey (Davies et al. 2018), consisting of a spectroscopic campaign currently being conducted on the Anglo-Australian Telescope, photometry (Davies et al. in prep.), and deep redshift catalogues, and stellar mass measurements from Thorne et al. (2020). These datasets are briefly described below.

REFERENCES

- Abraham R. G., van den Bergh S., 2001, *Science*, **293**, 1273
- Abraham R. G., van den Bergh S., Glazebrook K., Ellis R. S., Santiago B. X., Surma P., Griffiths R. E., 1996a, *ApJS*, **107**, 1
- Abraham R. G., Tanvir N. R., Santiago B. X., Ellis R. S., Glazebrook K., van den Bergh S., 1996b, *MNRAS*, **279**, L47
- Baldry I. K., Glazebrook K., Brinkmann J., Ivezić Ž., Lupton R. H., Nichol R. C., Szalay A. S., 2004, *ApJ*, **600**, 681
- Baldry I. K., Balogh M. L., Bower R. G., Glazebrook K., Nichol R. C., Bamford S. P., Budavari T., 2006, *MNRAS*, **373**, 469
- Baldry I. K., Glazebrook K., Driver S. P., 2008, *MNRAS*, **388**, 945
- Baldry I. K., et al., 2012, *MNRAS*, **421**, 621
- Bell E. F., et al., 2004, *ApJ*, **608**, 752
- Bellstedt S., et al., 2020, *MNRAS*, **496**, 3235
- Bernardi M., Shankar F., Hyde J. B., Mei S., Marulli F., Sheth R. K., 2010, *MNRAS*, **404**, 2087
- Brammer G. B., et al., 2009, *ApJ*, **706**, L173
- Brammer G. B., et al., 2011, *ApJ*, **739**, 24
- Brinchmann J., Charlot S., White S. D. M., Tremonti C., Kauffmann G., Heckman T., Brinkmann J., 2004, *MNRAS*, **351**, 1151
- Bruzual G., Charlot S., 2003, *MNRAS*, **344**, 1000
- Bundy K., Ellis R. S., Conselice C. J., 2005, *ApJ*, **625**, 621
- Caputi K. I., et al., 2015, *ApJ*, **810**, 73
- Cassata P., et al., 2008, *A&A*, **483**, L39
- Chabrier G., 2003, *PASP*, **115**, 763
- Charlot S., Fall S. M., 2000, *ApJ*, **539**, 718
- Cirasuolo M., et al., 2007, *MNRAS*, **380**, 585
- Conselice C. J., 2004, The Galaxy Structure-Redshift Relationship. p. 489, doi:10.1007/978-1-4020-2862-5_44
- Conselice C. J., Blackburne J. A., Papovich C., 2005, *ApJ*, **620**, 564
- Dale D. A., Helou G., Magdis G. E., Armus L., Díaz-Santos T., Shi Y., 2014, *ApJ*, **784**, 83
- Damjanov I., Zahid H. J., Geller M. J., Fabricant D. G., Hwang H. S., 2018, *ApJS*, **234**, 21
- Davidzon I., et al., 2017, *A&A*, **605**, A70
- Davies L. J. M., et al., 2015, *MNRAS*, **447**, 1014
- Davies L. J. M., et al., 2018, *MNRAS*, **480**, 768
- De Lucia G., Blaizot J., 2007, *MNRAS*, **375**, 2
- Driver S. P., Robotham A. S. G., 2010, *MNRAS*, **407**, 2131
- Driver S. P., et al., 2006, *MNRAS*, **368**, 414
- Driver S. P., et al., 2011, *MNRAS*, **413**, 971
- Driver S. P., Robotham A. S. G., Bland-Hawthorn J., Brown M., Hopkins A., Liske J., Phillips S., Wilkins S., 2013, *MNRAS*, **430**, 2622
- Driver S. P., et al., 2018, *MNRAS*, **475**, 2891
- Fontana A., et al., 2004, *A&A*, **424**, 23
- Fukugita M., et al., 2007, *AJ*, **134**, 579
- Hibbard J. E., Vacca W. D., 1997, *AJ*, **114**, 1741
- Hogg D. W., et al., 2002, *AJ*, **124**, 646
- Holwerda B. W., Dalcanton J. J., Radburn-Smith D., de Jong R. S., Guhathakurta P., Koekemoer A., Allen R. J., Böker T., 2012, *ApJ*, **753**, 25
- Huertas-Company M., et al., 2009, *A&A*, **497**, 743
- Huertas-Company M., et al., 2015, *ApJS*, **221**, 8
- Ilbert O., et al., 2010, *ApJ*, **709**, 644
- Ilbert O., et al., 2013, *A&A*, **556**, A55
- Jarvis M. J., et al., 2013, *MNRAS*, **428**, 1281
- Kauffmann G., et al., 2003, *MNRAS*, **341**, 33
- Kawinwanichakij L., et al., 2020, *ApJ*, **892**, 7
- Kelvin L. S., et al., 2014, *MNRAS*, **444**, 1647
- Knapen J. H., Beckman J. E., 1996, *MNRAS*, **283**, 251
- Koekemoer A., Fruchter A., Hack W., 2003, Space Telescope European Coordinating Facility Newsletter, **33**, 10
- Koekemoer A. M., et al., 2007, *ApJS*, **172**, 196
- Krywult J., et al., 2017, *A&A*, **598**, A120
- Lagos C. d. P., Tobar R. J., Robotham A. S. G., Obreschkow D., Mitchell P. D., Power C., Elahi P. J., 2018, *MNRAS*, **481**, 3573
- Lagos C. d. P., et al., 2019, *MNRAS*, **489**, 4196
- Laigle C., et al., 2016, *ApJS*, **224**, 24
- Lange R., et al., 2015, *MNRAS*, **447**, 2603
- Leja J., van Dokkum P. G., Franx M., Whitaker K. E., 2015, *ApJ*, **798**, 115
- Lilly S. J., et al., 2007, *ApJS*, **172**, 70
- Lintott C., et al., 2011, *MNRAS*, **410**, 166
- Madau P., Dickinson M., 2014, *ARA&A*, **52**, 415
- Mager V. A., Conselice C. J., Seibert M., Gusbar C., Katona A. P., Villari J. M., Madore B. F., Windhorst R. A., 2018, *ApJ*, **864**, 123
- McCracken H. J., et al., 2012, *A&A*, **544**, A156
- Moffett A. J., et al., 2016, *MNRAS*, **457**, 1308
- Mortlock A., et al., 2015, *MNRAS*, **447**, 2
- Muzzin A., et al., 2013, *ApJ*, **777**, 18
- Nair P. B., Abraham R. G., 2010, Vizier Online Data Catalog, p. J/ApJS/186/427
- Nelder J. A., Mead R., 1965, The computer journal, **7**, 308
- Obreschkow D., Murray S. G., Robotham A. S. G., Westmeier T., 2018, *MNRAS*, **474**, 5500
- Pannella M., Hopp U., Saglia R. P., Bender R., Drory N., Salvato M., Gabasch A., Feulner G., 2006, *ApJ*, **639**, L1
- Papovich C., Gialalisco M., Dickinson M., Conselice C. J., Ferguson H. C., 2003, *ApJ*, **598**, 827
- Peng Y.-j., et al., 2010, *ApJ*, **721**, 193
- Planck Collaboration et al., 2020, *A&A*, **641**, A6
- Pozzetti L., et al., 2010, *A&A*, **523**, A13
- R Core Team 2020, R: A Language and Environment for Statistical Computing. R Foundation for Statistical Computing, Vienna, Austria, <https://www.R-project.org/>
- Rawat A., Wadadekar Y., De Mello D., 2009, *ApJ*, **695**, 1315
- Renzini A., Peng Y.-j., 2015, *ApJ*, **801**, L29
- Robotham A. S. G., 2016a, Celestial: Common astronomical conversion routines and functions (ascl:1602.011)
- Robotham A. S. G., 2016b, magicaxis: Pretty scientific plotting with minor-tick and log minor-tick support (ascl:1604.004)
- Robotham A. S. G., et al., 2014, *MNRAS*, **444**, 3986
- Robotham A. S. G., Davies L. J. M., Driver S. P., Koushan S., Taranu D. S., Casura S., Liske J., 2018, *MNRAS*, **476**, 3137
- Robotham A. S. G., Bellstedt S., Lagos C. d. P., Thorne J. E., Davies L. J., Driver S. P., Bravo M., 2020, *MNRAS*, **495**, 905
- Sandage A., 2005, *ARA&A*, **43**, 581
- Scarlata C., et al., 2007a, *ApJS*, **172**, 406
- Scarlata C., et al., 2007b, *ApJS*, **172**, 494
- Schechter P., 1976, *ApJ*, **203**, 297
- Scodreggio M., et al., 2018, *A&A*, **609**, A84
- Scoville N., et al., 2007, *ApJS*, **172**, 150
- Siudek M., et al., 2018, *A&A*, **617**, A70
- Strateva I., et al., 2001, *AJ*, **122**, 1861
- Taniguchi Y., et al., 2007, *ApJS*, **172**, 9
- Taylor-Mager V. A., Conselice C. J., Windhorst R. A., Jansen R. A., 2007, *ApJ*, **659**, 162
- Taylor V. A., Jansen R. A., Windhorst R. A., Odewahn S. C., Hibbard J. E., 2005, *ApJ*, **630**, 784
- Taylor E. N., et al., 2009, *ApJ*, **694**, 1171
- Taylor E. N., et al., 2015, *MNRAS*, **446**, 2144
- Thorne J. E., et al., 2020, arXiv e-prints, p. arXiv:2011.13605
- Tomczak A. R., et al., 2014, *ApJ*, **783**, 85
- Trayford J. W., Theuns T., Bower R. G., Crain R. A., Lagos C. d. P., Schaller M., Schaye J., 2016, *MNRAS*, **460**, 3925
- Vergani D., et al., 2008, *A&A*, **487**, 89
- Weigel A. K., Schawinski K., Bruderer C., 2016, *MNRAS*, **459**, 2150

- Whitaker K. E., et al., 2014, [ApJ](#), **795**, 104
 Whitaker K. E., et al., 2015, [ApJ](#), **811**, L12
 Willett K. W., et al., 2017, [MNRAS](#), **464**, 4176
 Williams R. J., Quadri R. F., Franx M., van Dokkum P., Labbé I., 2009, [ApJ](#), **691**, 1879
 Windhorst R. A., et al., 2002, [ApJS](#), **143**, 113
 Wright A. H., et al., 2017, [MNRAS](#), **470**, 283
 Wright A. H., Driver S. P., Robotham A. S. G., 2018, [MNRAS](#), **480**, 3491
 van den Bergh S., Abraham R. G., Ellis R. S., Tanvir N. R., Santiago B. X., Glazebrook K. G., 1996, [AJ](#), **112**, 359
 van der Wel A., et al., 2012, [ApJS](#), **203**, 24

9 APPENDIX A: RANDOM SAMPLES OF THE MORPHOLOGICAL TYPES.

Here we show 49 random galaxies in each of our morphological categories (BD,D,E,H,C). We show our stamps in both HST/F814W filter and Subaru *gri*.

10 APPENDIX B: BEST SCHECHTER FIT PARAMETERS.

This table shows our best Schechter fit parameters of the total and morphological SMFs, shown in Figure 12.

11 THE NON-LSS-CORRECTED EVOLUTION OF THE SMD

Figure 22 shows the evolution of the integrated stellar mass density, ρ_* before we apply our large scale structure corrections (reported in Table 4 and shown in Figure 11). This is to further confirm that the corrections do not derive the overall trends that we find in Figure 15 as explained in Section 4.

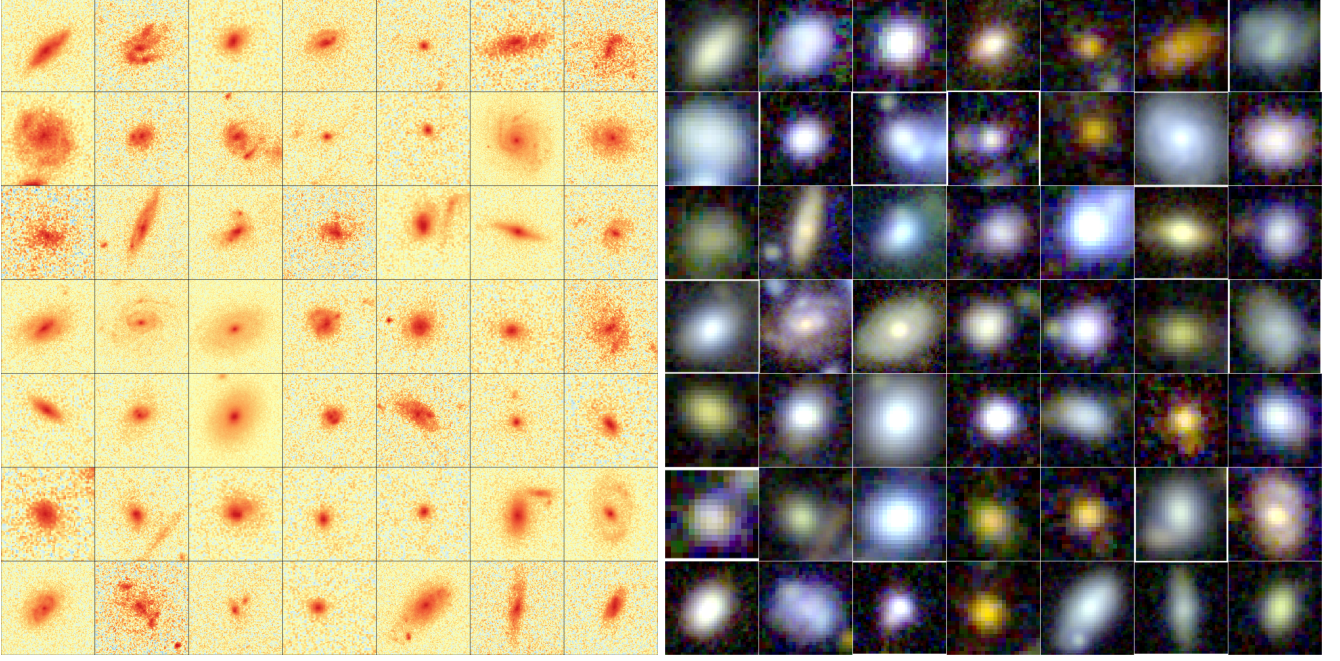


Figure 17. Random sample of double component systems. Left set of panels: ACS/F814W image. Right set of panels: SUBARU *gri* combined image.

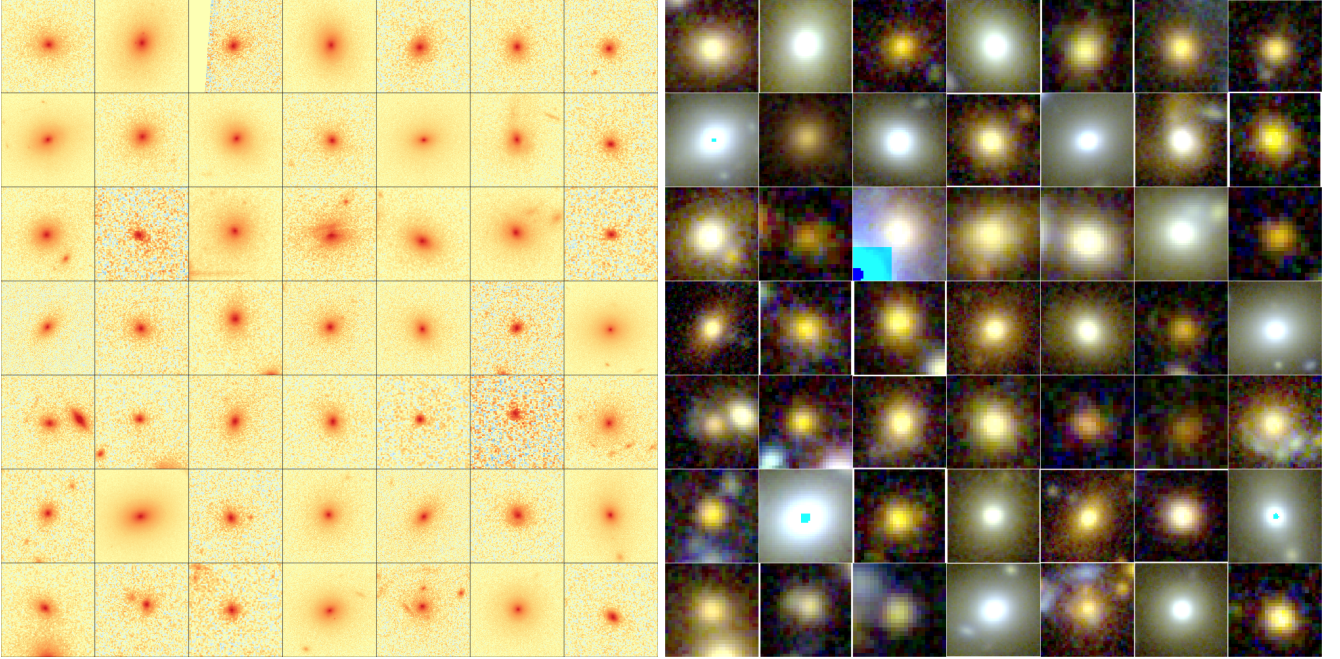


Figure 18. Random sample of elliptical systems. Left set of panels: ACS/F814W image. Right set of panels: SUBARU *gri* combined image.

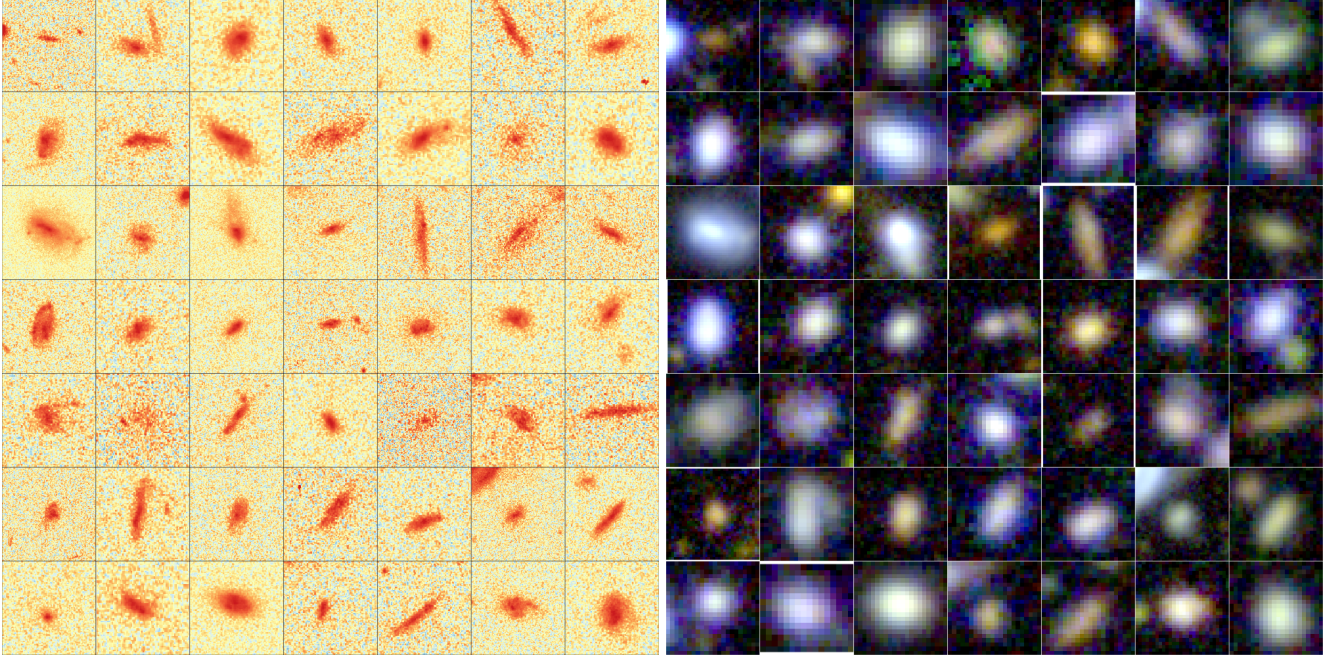


Figure 19. Random sample of pure disk systems. Left set of panels: ACS/F814W image. Right set of panels: SUBARU *gri* combined image.

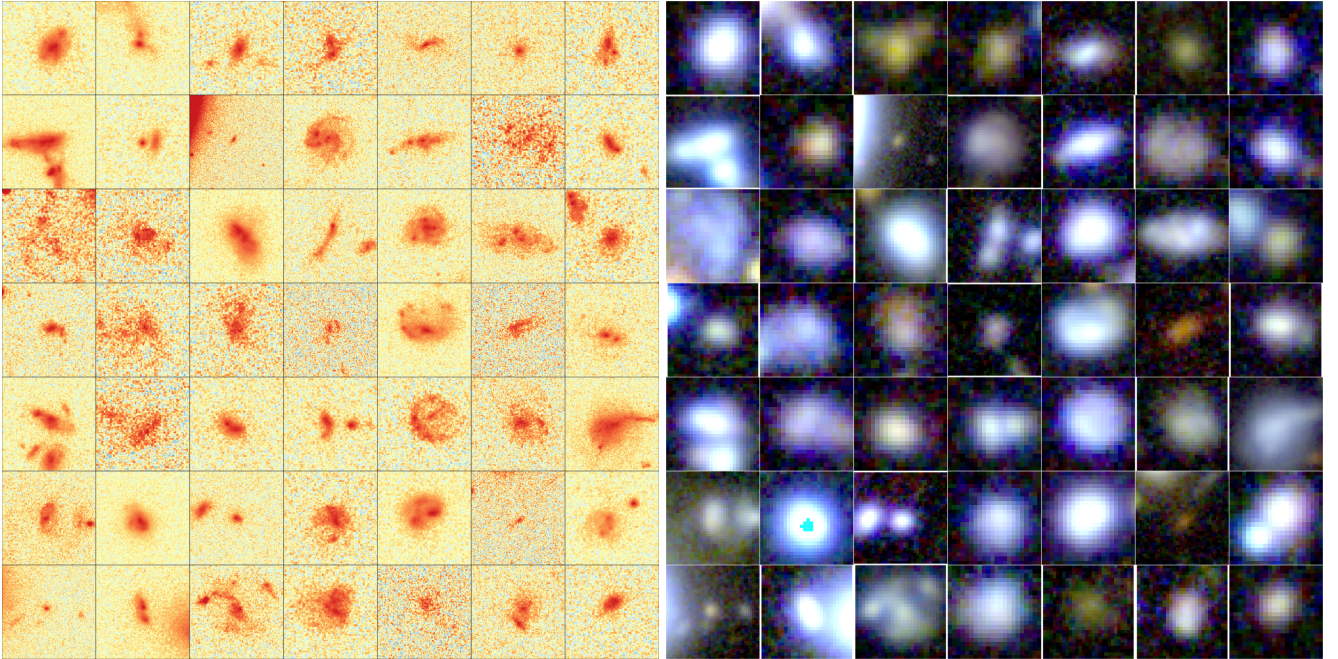


Figure 20. Random sample of complex systems (*hard*). Left set of panels: ACS/F814W image. Right set of panels: SUBARU *gri* combined image.

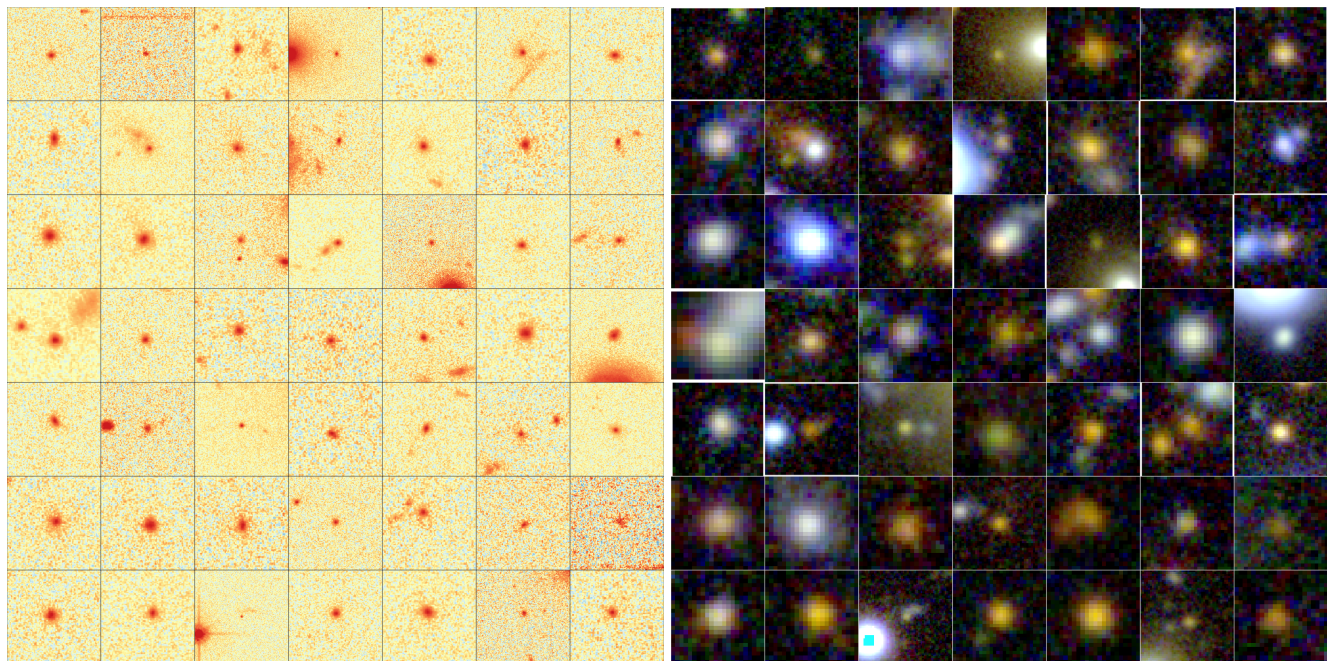


Figure 21. Random sample of low angular sized systems (*compact*). Left set of panels: ACS/F814W image. Right set of panels: SUBARU *gri* combined image.

Table 6. Best Schechter fit parameters of *total* and different morphological types in different redshift bins.

<i>z</i> -bins	$0.0 \leq z < 0.08$	$0.0 \leq z < 0.25$	$0.25 \leq z < 0.45$	$0.45 \leq z < 0.60$	$0.60 \leq z < 0.70$	$0.70 \leq z < 0.80$	$0.80 \leq z < 0.90$	$0.90 \leq z \leq 1.00$
Total (Double Schechter)								
$\log_{10}\Phi_1^*$	-2.43 ± 0.04	-2.68 ± 0.07	-2.55 ± 0.03	-2.66 ± 0.07	-2.71 ± 0.08	-2.61 ± 0.03	-2.73 ± 0.04	-2.81 ± 0.04
$\log_{10}M^*$	10.65 ± 0.04	10.96 ± 0.06	10.83 ± 0.03	10.76 ± 0.06	10.79 ± 0.05	10.66 ± 0.04	10.76 ± 0.04	10.84 ± 0.04
α_1	-0.04 ± 0.22	-1.08 ± 0.08	-0.79 ± 0.09	-0.32 ± 0.30	-0.22 ± 0.33	0.15 ± 0.20	-0.02 ± 0.21	-0.23 ± 0.20
$\log_{10}\Phi_2^*$	-3.11 ± 0.21	-8.90 ± 4.85	-4.76 ± 0.55	-3.11 ± 0.23	-3.14 ± 0.26	-3.26 ± 0.14	-3.22 ± 0.15	-3.32 ± 0.16
α_2	-1.56 ± 0.16	-5.06 ± 3.27	-2.62 ± 0.36	-1.48 ± 0.15	-1.36 ± 0.17	-1.61 ± 0.11	-1.36 ± 0.11	-1.43 ± 0.10
Total (Single Schechter)								
$\log_{10}\Phi^*$	-2.60 ± 0.03	-2.74 ± 0.06	-2.77 ± 0.03	-2.77 ± 0.03	-2.78 ± 0.03	-2.85 ± 0.03	-2.83 ± 0.02	-2.94 ± 0.2
$\log_{10}M^*$	10.93 ± 0.03	11.01 ± 0.05	11.00 ± 0.03	10.98 ± 0.03	10.99 ± 0.02	11.03 ± 0.02	11.02 ± 0.02	11.08 ± 0.02
α	-1.04 ± 0.03	-1.15 ± 0.05	-1.16 ± 0.02	-1.17 ± 0.03	-1.05 ± 0.02	-1.12 ± 0.02	-1.00 ± 0.02	-1.10 ± 0.02
Double								
$\log_{10}\Phi^*$	-2.60 ± 0.03	-2.61 ± 0.06	-2.68 ± 0.03	-2.73 ± 0.03	-2.75 ± 0.02	-2.82 ± 0.02	-2.90 ± 0.02	-3.05 ± 0.02
$\log_{10}M^*$	10.75 ± 0.03	10.71 ± 0.05	10.78 ± 0.03	10.78 ± 0.03	10.77 ± 0.02	10.82 ± 0.02	10.83 ± 0.02	10.90 ± 0.02
α	-0.87 ± 0.04	-0.95 ± 0.07	-0.90 ± 0.03	-0.80 ± 0.04	-0.55 ± 0.04	-0.59 ± 0.04	-0.42 ± 0.03	-0.55 ± 0.03
Pure-Disk								
$\log_{10}\Phi^*$	-4.32 ± 0.38	-3.12 ± 0.23	-4.09 ± 0.23	-3.55 ± 0.12	-3.52 ± 0.09	-3.45 ± 0.08	-3.23 ± 0.04	-3.21 ± 0.04
$\log_{10}M^*$	10.82 ± 0.22	10.00 ± 0.18	10.76 ± 0.14	10.74 ± 0.08	10.78 ± 0.06	10.79 ± 0.06	10.71 ± 0.03	10.75 ± 0.03
α	-2.12 ± 0.13	-1.04 ± 0.46	-1.96 ± 0.09	-1.68 ± 0.07	-1.54 ± 0.05	-1.52 ± 0.05	-1.24 ± 0.04	-1.24 ± 0.03
Elliptical								
$\log_{10}\Phi^*$	-2.99 ± 0.03	-3.23 ± 0.08	-3.20 ± 0.04	-3.24 ± 0.04	-3.23 ± 0.03	-3.26 ± 0.02	-3.35 ± 0.02	-3.45 ± 0.02
$\log_{10}M^*$	10.87 ± 0.04	11.14 ± 0.09	11.00 ± 0.04	10.89 ± 0.05	10.88 ± 0.04	10.78 ± 0.04	10.87 ± 0.03	10.93 ± 0.03
α	-0.37 ± 0.07	-0.71 ± 0.10	-0.61 ± 0.05	-0.40 ± 0.08	-0.25 ± 0.07	0.09 ± 0.09	-0.07 ± 0.07	-0.03 ± 0.07
Compact								
$\log_{10}\Phi^*$	—	-19.91 ± 45.11	-4.01 ± 1.14	-9.70 ± 62.46	-4.76 ± 0.89	-3.31 ± 0.20	-4.72 ± 0.32	-4.69 ± 0.24
$\log_{10}M^*$	—	8.37 ± 0.74	9.79 ± 0.51	12.71 ± 32.57	10.37 ± 0.41	9.67 ± 0.17	10.73 ± 0.20	10.86 ± 0.16
α	—	17.85 ± 35.50	-2.09 ± 1.37	-2.90 ± 0.28	-2.29 ± 0.42	-1.16 ± 0.62	-1.79 ± 0.15	-1.75 ± 0.11
Hard								
$\log_{10}\Phi^*$	-5.34 ± 0.94	-5.42 ± 2.50	-6.72 ± 1.60	-5.06 ± 0.40	-5.36 ± 0.37	-4.73 ± 0.24	-4.42 ± 0.12	-4.29 ± 0.10
$\log_{10}M^*$	11.06 ± 0.70	11.00 ± 1.56	12.34 ± 1.43	11.40 ± 0.33	11.74 ± 0.33	11.22 ± 0.19	11.21 ± 0.11	11.16 ± 0.09
α	-1.35 ± 0.69	-2.01 ± 0.75	-1.97 ± 0.14	-1.67 ± 0.13	-1.64 ± 0.10	-1.55 ± 0.10	-1.27 ± 0.07	-1.29 ± 0.06

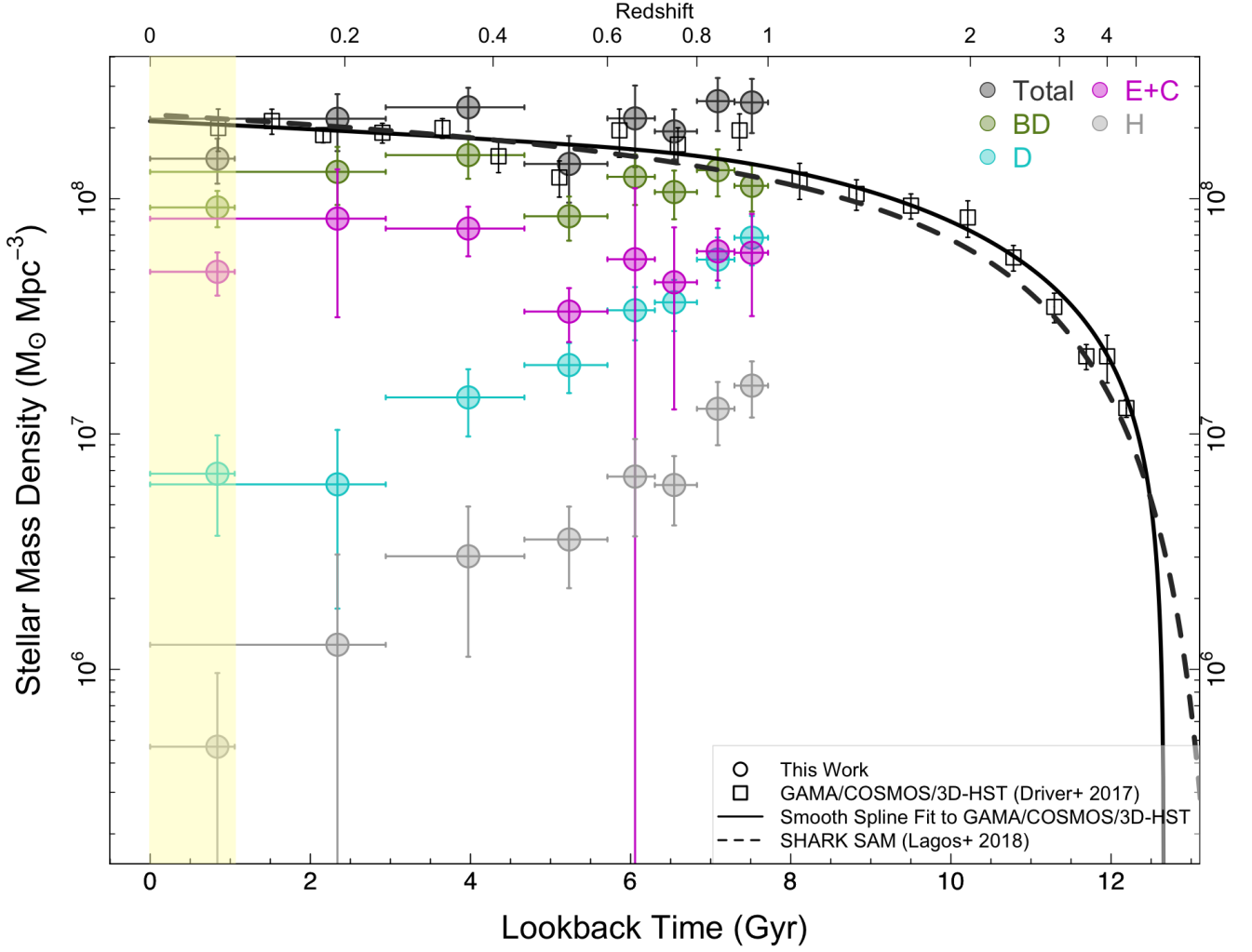


Figure 22. The evolution of the stellar mass density (SMD) of total and morphological types before applying the LSS corrections. Highlighted region shows the epoch covered by the GAMA data.